# Atmospheric pressure plasma activation of water droplets

## Juliusz Kruszelnicki[1] , Amanda M Lietz[1] and Mark J Kushner[2,3]

[1] Department of Nuclear Engineering and Radiological Sciences, University of Michigan, 2355 Bonisteel Blvd., Ann Arbor, MI 48109-2104, United States of America
[2] Department of Electrical Engineering and Computer Science, University of Michigan, 1301 Beal Ave., Ann Arbor, MI 48109-2122, United States of America

E-mail: jkrusze@umich.edu, lietz@umich.edu and mjkush@umich.edu

## Abstract

Low temperature plasma treatment of water is being investigated due to its use in pollution abatement, wound treatment and agriculture. Plasma produced reactive oxygen and nitrogen species (RONS) are formed in the gas phase and solvate into the liquid. Activation of the liquid is often limited by transport of these RONS to the liquid surface. Micrometer scale droplets immersed in the plasma have a large surface to volume ratio, which increases the interaction area for a given volume of water, and can increase the rates of transport from the gas to liquid. In this paper, results from 0 and 2D modeling of air-plasma activation of water micro-droplets are discussed. The solvation dynamics are sensitive to the Henry's law constant ($h$) of each species, which describes its hydrophobicity (low $h$) or hydrophilicity (high $h$). The liquid densities of stable species with high $h$ values (e.g. $H_2O_2$, $HNO_x$) are sensitive to droplet diameter. For large droplets, hydrophilic species may deplete the gas-phase inventory of RONS before liquid-phase saturation is reached, limiting the total in-liquid density for species with high $h$. For smaller droplets, higher average in-droplet densities of these species can be produced. Liquid concentrations of stable species with low $h$ (e.g. $O_3$, $N_2O$, $H_2$) had a weak dependence on droplet size as droplets are quickly saturated and solvation does not deplete the gas phase. An analysis of this behavior is discussed using the well-stirred reactor (0D) approximation. Spatial non-uniformity of the plasma also has an impact on the solvation rates and kinetics. Gas phase depletion of high-$h$ species leads to a decrease in solvation rates. Low-$h$ species that saturate the surface of the droplets during plasma-on periods can quickly de-solvate in the afterglow.

Keywords: plasma activation water droplets, plasma chemistry, plasma-water interactions

(Some figures may appear in colour only in the online journal)

## 1. Introduction

Low temperature atmospheric pressure plasmas (APPs) interacting with liquids are being investigated for biomedical, agricultural, materials synthesis and water treatment applications [1]. From a pollutant remediation perspective, plasma acts as an advanced oxidation method, enabling its use to address a variety of pollutants [2–4]. From a biomedical perspective, beneficial effects of plasma treated liquids are generally attributed to the production of reactive oxygen and nitrogen species (RONS) by the plasma which solvate and further react in the liquid [5–12].

For example, $H_2O_{2aq}$ can act as either an oxidant (reduction potential $E^0 = 1.77$ V) or a reductant ($E^0 = -0.70$ V) [13]. (The 'aq' subscript denotes a solvated or in-liquid aqueous species.) The oxidation probability of a species is measured by its reduction potential, $E^0$, which describes the propensity to acquire electrons in a solution. $E^0$ is analogous to pH as means of determining proton transfer. $H_2O_{2aq}$ may produce DNA damage and oxidize lipids and proteins, thereby affecting

---

[3] Author to whom any correspondence should be addressed.

the viability of human cells [14]. $H_2O_{2aq}$ reacts with nitrite ($NO_{2aq}^-$) to form peroxinitrite ($ONOO_{aq}^-$) which can affect the physiology of living cells and can participate in catalytic processes which affects abatement of water pollutants [15–17].

Ozone, an oxidative product of discharges in air with $E^0 = 2.07$ V, is relatively stable in water with a half-life of thousands of seconds in the absence of impurities such as organics [13, 18]. Ozone is effective in abating a wide range of micro-pollutants, pharmaceutical compounds, pesticides and endocrine disruptors from water [19]. The direct reactions between ozone and organic compounds in water are often pH-dependent [20]. Since plasma treatment may reduce the pH of liquids, regulating pH of the liquid by plasma exposure may enable additional control over liquid kinetics and selectivity [21].

APPs in humid mixtures produce hydroxyl radicals, which are the strongest oxidant in aqueous solutions, with $E^0 = 2.85$ V [13]. This large reduction potential enables $OH_{aq}$ to degrade a variety of chemical compounds, including phenol and aromatic hydrocarbons, organic dyes, and aliphatic compounds [13]. $OH_{aq}$ attacks outer cell membranes enabling microbial decontamination of water and surfaces [13, 22]. The reactivity of $OH_{aq}$ results in formation of numerous secondary species [6].

Many types of low temperature plasma sources have been experimentally investigated for water treatment [23–29]. Modeling efforts have addressed the kinetics and dynamics of plasma-liquid interactions [26, 30–33]. The majority of plasma sources for treating liquids are designed to keep the temperatures of both the gas and liquid low, as the liquids being treated (or in the case of biomedical applications, the tissue lying under the liquid) are often heat sensitive. When the liquid (or contacting surface) is not heat sensitive, higher specific power can be used. Low temperature plasma sources investigated for sterilization or water treatment include a plasma jet impinging onto a water surface, a pin to pin discharge in liquid water, discharges sustained in bubbles, two phase gliding arc discharges, and treatment of films of water flowing through a dielectric barrier discharge (DBD) [34–38].

Many water treatment applications require processing large volumes of water while in other applications treatment is more focused on producing high concentrations of RONS. In either case, activation of the liquid is typically transport limited. The activating species must first transport from their site of creation in the plasma to the surface of liquid, the species must then transport into the liquid and finally transport from the surface of the liquid into the interior. Many of these transport limits can be addressed by activation of small liquid droplets immersed in the plasma. In this plasma activation scheme, radicals and ions are produced in the immediate vicinity of the droplet, thereby minimizing transport limits to the liquid surface. The large surface-to-volume ratio (SVR) of small droplets then minimizes transport limits from the surface of the liquid into the bulk of the liquid. Several experimental studies have shown efficient plasma activation of droplets compared to treatment of bulk liquids. For example, plasma treatment of droplets by electrospray of water has been found to be effective for inactivation of biofilms [22, 38]. Plasma treated water

mist has effectively sterilized *E. coli* and influenced the production of RONS in the liquid [39]. Plasma treatment of water droplets has also produced particularly high concentrations of $H_2O_{2aq}$ [40, 41].

In this paper, results are discussed from a computational investigation of plasma treatment of water droplets. Fundamental scaling laws and plasma chemistry of the air plasma-water droplet system are investigated using global models and analytical analysis. Results from 2D modeling which incorporates the consequences of electrodynamics, anisotropy and local transport are also discussed. Droplets were exposed to a series of hundreds of pulses, followed by an afterglow period. We found that the primary neutral reactive species produced in the droplets are acids, $HO_{2aq}$, $H_2O_{2aq}$, and $O_{3aq}$. Hydroxyl radicals were also formed at high rates during the plasma-on periods, however, these radicals were generally confined to the surface of the droplets due to their high reactivity and short lifetime. The primary terminal species were $NO_{3aq}^-$, and $H_3O_{aq}^+$, the high densities of which led a significant decrease in the pH of the water droplets to as low as pH $\approx 1$ at droplet diameters of 5 $\mu$m. The surface-to-volume-ratio (SVR) significantly impacts the final average densities of species having a high Henry's law constant, $h$. Conversely, densities of aqueous hydrophobic species with low $h$ showed little dependence on the diameter of the droplets. This selectivity based on $h$ could provide additional avenues to selectively control liquid kinetics. The spatially-resolved 2D modeling further showed that aqueous species which had reached their saturation densities at the surface of the droplet during plasma pulsing in filamentary discharges may de-solvate at high rates in the afterglow to maintain gas–liquid equilibrium. Control over the size and distribution of droplets, as well as uniformity of the plasma, are therefore critical for efficient transfer of the desired reactive plasma species to and from the liquid, and retention of reactants in the droplet.

The models are described in section 2. The reaction mechanisms and initial conditions are discussed in section 3. Results from global modeling including the dynamics of the base case, the effect of droplet diameter, the role of depletion of species from the gas phase, and the number of droplets are discussed in section 4. Results from the 2D model for reactive species transport are discussed in section 5. Concluding remarks are in section 6.

## 2. Description of the models

### 2.1. Global model

*GlobalKin* is a 0D plasma chemistry model which has been extended to address plasma-liquid interactions. Detailed descriptions of the model and the manner of treating liquids appear in [42] and so only brief descriptions will be provided here. *GlobalKin* represents the plasma-liquid system as two well-mixed volumes, one for the plasma and a second for the liquid, which interact through a surface of specified area. Transport of species from the volumes of both plasma and liquid to the interfacial surface are described by their respective diffusion coefficients in that medium and diffusion length

J. Phys. D: Appl. Phys. **52** (2019) 355207

J Kruszelnicki *et al*

of the plasma or liquid. In this investigation, the global model represents a DBD by specifying power deposition in the plasma during a 10 ns period. The electron temperature is calculated by the electron energy conservation equation, including power deposition from the applied electric field and losses due to electron impact processes. The stationary Boltzmann's equation is solved using a 2-term spherical harmonic expansion for the electron energy distribution for a range of $E/N$ (electrical field/gas number density) values. A lookup table is generated from these results for electron impact rate coefficients and transport coefficients as a function of the electron temperature. This table can be updated periodically during the simulation to reflect changes in composition of the gas, however this procedure was not necessary here due to the low dissociation fraction of the background gases. The gas temperature is calculated assuming a fixed wall temperature.

In *GlobalKin*, the rate equation for the density of gas phase species is

$$\frac{dn_i}{dt} = \sum_j \left\{ \left( a_{ij}^{(R)} - a_{ij}^{(L)} \right) k_j \prod_l n_l^{a_{lj}^{(L)}} \right\}$$
$$+ \sum_m \left\{ -\frac{D_i n_i}{\Lambda^2} f_m S_{im} + \sum_k \frac{D_k n_k}{\Lambda^2} f_m S_{km} g_{ikm} \right\} \quad (1)$$

where $n_i$ is the number density of species $i$. The first term represents the gas phase reactions $j$ which are sources or losses of species $i$. $a_{ij}^{(R)}$ and $a_{ij}^{(L)}$ are the number of molecules of species $i$ which are on the right hand side and the left hand side of reaction $j$. The second term represents diffusion losses to bounding surfaces, including recombination of charged species. Several bounding surfaces, $m$, can be represented having different fractional areas in contact with the plasma, $f_m$, and different reaction probabilities, $S_{im}$. The first part of this term is for losses due to reactions of species $i$ having diffusion coefficient $D_i$ on material $m$. $\Lambda$ is the diffusion length of the plasma portion of the reactor. The second part represents the sources of species $i$ due to surface reactions of species $k$ on material $m$ which returns a fraction $g_{ikm}$ of species $i$ for every molecule of species $k$. The reaction probability, $S_{km}$, is the fraction of the diffusion flux which disappears at the wall, and the give fraction, $g_{ikm}$, is the fraction of the consumed flux of species $k$ which returns as species $i$.

From the perspective of the plasma in *GlobalKin*, the liquid is a surface in contact with the plasma having a reaction probability that is updated dynamically depending on the concentration of a species in the liquid. The loss of plasma species diffusing out of the plasma volume to and reacting at the liquid surface represents a source of species into the liquid volume. Charged species have a unity reaction probability and solvate. Although it is possible for ions to neutralize at the surface and reflect back into the gas phase as neutral, this process was not included in the model. From a practical perspective, this sequence does occur in the model. Ions solvating into the liquid are neutralized by charge exchange (or other processes), become a super-saturated neutral which then desolvates (see discussion below).

The reaction probabilities of neutral species are bounded by the density of their liquid or gas phase counterpart relative to equilibration concentrations given by Henry's law. For liquid surface $m$ in contact with the plasma,

$$S_{im} = \alpha \cdot \max \left( \frac{h_i n_{i,g} - n_{i,l}}{h_i n_{i,g}}, 0 \right), \quad (2)$$

where $S_{im}$ is the reaction probability of species $i$ on the liquid surface, $h_i$ is the unitless Henry's law equilibrium constant for species $i$, $n_{i,g}$ and $n_{i,l}$ are the volume-averaged number density of species $i$ in the gas and the liquid; and $\alpha$ is the mass accommodation coefficient. This reaction probability will trend towards zero with the density of species in the gas and liquid phases are at their equilibrium values. If the liquid is oversaturated ($n_{i,l} > h n_{i,g}$) then the flux from the liquid surface into the gas phase is given by:

$$\Gamma_i = \frac{D_i(n_{i,l} - h_i n_{i,g})}{\Lambda^2} \frac{V_g}{A_l}. \quad (3)$$

The solvation and de-solvation rates described by equations (2) and (3) are simplifying assumptions. In reality, the kinetics of this process can be influenced by an adsobed layer at the interface, and potential energy barriers of desolvation which vary by species [43].

The mass accommodation coefficient, $\alpha$, is the probability that a molecule impinging on an unsaturated liquid surface solvates [44, 45]. This coefficient is analogous to a sticking coefficient for a radical on a solid material. Experimentally and computationally derived values of $\alpha$ range from 0.001 to 1.0 [44]. For example, values of $\alpha$ for ambient temperatures on 200 $\mu$m water droplets range from 0.04 $N_2O_5$ to 0.16 for $HNO_3$ [46]. Due to the limited availability of data, we assumed $\alpha = 1$ for all species. With this simplification, we will overestimate of the rate of solvation for species having $\alpha$ significantly less than 1 when the value of $n_{i,l}$ is low, solvation is not limited by Henry's law considerations and solvation is not transport limited. However, the saturated values of solvated species will weakly depend on $\alpha$.

The density of liquid species are calculated by:

$$\frac{dn_{i,l}}{dt} = \sum_j \left\{ \left( a_{ij}^{(R)} - a_{ij}^{(L)} \right) k_j \prod_l n_l^{a_{lj}^{(L)}} \right\}$$
$$+ \frac{D_i n_{i,g}}{\Lambda^2} f_l S_{i,liquid} \frac{V_g}{V_l} - \max \left\{ 0, \frac{D_i (n_{i,l} - h_i n_{i,g})}{\Lambda^2} \frac{V_g}{V_l} \right\}, \quad (4)$$

where $n_{i,l}$ is the number density of liquid species $i$. The first term represents reactions occurring inside the liquid. The second term is for solvation into the liquid of the gas phase counterpart, $n_{i,g}$. $V_g$ is the plasma volume, and $V_l$ is the liquid volume. The third term is a loss from the liquid to the gas phase if the liquid is oversaturated with that species. Evaporation from the liquid into the gas is included. The flux from the liquid surface of the evaporating species (in this case $H_2O$) is

$$\Gamma_{i,e} = \frac{D_i(n_{i,s} - h_i n_{i,g})}{\Lambda^2} \frac{V_g}{A_l} \quad (5)$$

**Table 1.** Henry's law constants [41].

| Species | h (unitless) | Note |
|---|---|---|
| $H_2O_2$ | $1.92 \times 10^6$ | |
| $HO_2$ | $1.32 \times 10^5$ | |
| OH, $OH(A^2\Sigma)$ | 620 | a |
| H, $H^*$ | $6.00 \times 10^3$ | a |
| $H_2$, $H_2(r)$, $H_2(v)$, $H_2^*$ | $1.9 \times 10^{-2}$ | a |
| $H_2O(v)$ | 1 | b |
| O, $O(^1D)$ | 1 | a,b |
| $O_2$, $O_2(r)$, $O_2(v)$, $O_2(^1\Delta_g)$, $O_2(^1\Sigma_u)$ | $3.24 \times 10^{-2}$ | a |
| $O_3$, $O_3^*$ | 0.274 | |
| $N_2$, $N_2(r)$, $N_2(v)$, $N_2^*$, $N_2^{**}$, N, $N(^2D)$ | $1.6 \times 10^{-2}$ | a |
| $N_2O_3$ | 600 | |
| $N_2O_4$ | 37.0 | |
| $N_2O_5$ | 48.5 | |
| $N_2O$, $N_2O(v)$ | 0.599 | a |
| $HO_2NO_2$ | $9.73 \times 10^4$ | |
| NO | $4.4 \times 10^{-2}$ | |
| $NO_2$ | 0.28 | |
| $NO_3$ | 41.5 | |
| $HNO_2$, HNO | $1.15 \times 10^3$ | a |
| $HNO_3$, ONOOH | $4.80 \times 10^6$ | |
| CO, CO(v) | $2.42 \times 10^{-2}$ | a |
| $CO_2$, $CO_2(v)$ | 0.823 | a |
| NH | $1.47 \times 10^3$ | c |

a Value corresponds to the first species in the list. Other species were assumed to have the same Henry's law constant.
b Approximated. Species reacts quickly in water and will not reach Henry's law saturation.
c Approximated by analogy to $NH_3$.

where $n_{i,s}$ is the gas number density corresponding to the saturated vapor pressure of the liquid. Losses by evaporation from the liquid are assumed to be negligible and so the liquid volume does not change. Our approach to evaporation implemented by equation (5) is a simplifying assumption, while more detailed studies of aerosol evaporation have been performed with and without the presence of plasma [33, 47]. The gas phase conditions in our studies have 100% relative humidity and the gas heating is small; and so we do not expect this simplifying assumption to have a major effect on our results. Our approach also does not consider additional factors impacting adsorption and solvation, such as changes in surface tension or desorption energy barriers [43]. While these factors are important under select conditions, we lack the fundamental data to implement these higher order effects in a systematic way for all species. Our approach which limits fluxes to and from the droplet based on Henry's law equilibrium at the surface is an approximation which has the advantage of being systematically applicable with the available data. The Henry's law constants used in both the 0D and 2D simulations are listed in table 1. These values were taken primarily from work by Sander in [48] with extensions described in [42].

### 2.2. 2D model

While global modeling is useful in addressing large reaction mechanisms and long timescales to propose general scaling laws, transport limits are difficult to assess. For example, by assuming the plasma is represented by a well-stirred reactor, the plasma is functionally a diffuse glow rather than having a filamentary structure as often occurs at atmospheric pressure. Transport from the volumes of the plasma and liquid to their shared boundary does not take into account spatial gradients (other than generically by use of the diffusion length). With the liquid being well stirred, saturation of the liquid occurs on a volume averaged basis, which does not capture the transport limits that occur when only the surface is saturated. Processes such as surface ionization waves (SIWs) often occur on dielectric-like surfaces (as is low conductivity water). SIWs produce reactivity in the immediate proximity of the liquid, a phenomenon that is also not well addressed by global modeling. Despite these limitations, the scaling laws produced by global modeling provide keen insights into the reaction mechanisms; and provide a useful and practical framework for optimizing and tuning the activation of droplets. However, investigation of spatially dependent phenomena requires higher order modeling.

The spatially-resolved results in this computational investigation were obtained using the multi-fluid plasma hydrodynamics model, *nonPDPSIM*, which addresses atmospheric pressure plasma activation of liquids. The algorithms and methods of solution for gas phase processes are discussed in detail in [49]. The algorithms and method of solution for the gas phase plasma interacting with a liquid are discussed in detail in [50]. These algorithms will be only briefly discussed here.

The continuity equations for charged particles in the plasma and liquid, and surfaces charges on solids are implicitly integrated simultaneously with Poisson's equation for the electric potential on an unstructured mesh. The continuity equation for species $i$ is

$$\frac{\partial n_i}{\partial t} = -\nabla \cdot \vec{\Gamma}_i + S_i + \left[\sum_m -\nabla \cdot \vec{\Gamma}_m \gamma_m\right]_b, \quad (6)$$

where $n_i$ is the number density and $\Gamma_i$ is the flux of species $i$. The source due to collisions is $S_i$. The term in brackets only applies to electrons at nodes adjacent to solid surfaces where electrons are produced by secondary electron emission from surfaces by ions with probability $\gamma_m$ for species $m$. The secondary yield was $\gamma_m = 0.1$ for positive ions. (Photo-electron emission was not included.) Fluxes of charged particles are given by the Scharfetter and Gummel method that automatically provides fluxes as either upwind or downwind [51, 52].

The electric potential $\Phi$ is produced from the solution of Poisson's equation,

$$\nabla \cdot (\varepsilon \nabla \Phi) = -\left(\sum_i q_i n_i + \rho_M\right), \quad (7)$$

where $\varepsilon$ is the permittivity appropriate for plasma, liquid or solid regions, $q_j$ is the elementary charge, and $\rho_M$ is the charge on solid surfaces and in materials. The permittivity of the gas phase is $\varepsilon_0$ (permittivity of free space) while that of water is $80\varepsilon_0$.

Following an update of charged particle densities and electric potential, the electron temperature is updated using the electron energy conservation equation,

$$\frac{\partial}{\partial t}\left(\frac{3}{2}n_e k_B T_e\right) = S_P(T_e) - L_P(T_e)$$
$$- \nabla \cdot \left(\frac{5}{2}\Gamma_e k_B T_e - \kappa(T_e) \cdot \nabla T_e\right), \qquad (8)$$

where $T_e$ is the electron temperature, $n_e$ is the electron density, $k_B$ is Boltzmann's constant, $\kappa$ is the electron thermal conductivity, $S_P$ is the sources of power, in this case, Joule heating from the electric field and $L_P$ represents collisional losses or gains in energy. In this study, the ion temperatures are assumed to be equal to the gas temperature due to high rates of collisions at atmospheric pressure.

Transport of neutrals is calculated using species-specific, local diffusion coefficient everywhere except for the liquid–gas boundary region. In this study, convection in the gas and liquid are not considered. The specific transport calculation performed at the gas–liquid boundary is described below. Radiation transport is performed using a Green's function formulation to provide fluxes from each node to a set of neighbors within its line-of-sight. Photoionization of $O_2$ by photons emitted by excited nitrogen species ($N_2(C^3\Pi)$ and $N_2(E^3\Sigma)$) was included. The non-ionizing absorption cross sections in the base case were $1 \times 10^{-18}$ cm$^2$ for $O_2$ and $N_2$, and $3 \times 10^{-17}$ cm$^2$ for $H_2O$, while the ionization cross section was assumed to be $1 \times 10^{-19}$ cm$^2$ [53]. No photoionization of the liquid species was included in these cases.

The treatment of liquids in *nonPDPSIM* will be briefly described. Liquids are designated to occupy a fixed region within the mesh. All of the algorithms described above for the plasma are also used in liquid regions, while using reaction mechanisms, permittivities and transport coefficients appropriate for the liquid, in this case water. This equal treatment of species transport enables self-consistent calculation of potentials and charge distributions. Transport of species between the gas and liquid is addressed similarly to *GlobalKin* while spatially resolving the process. Gas species entering the liquid region solvate either immediately if they have a liquid-phase counterpart (e.g. $O_2 \rightarrow O_{2aq}$) or through solvation reaction with the dominant liquid species—in this case $H_2O_{aq}$ (e.g. $H_5O_2^+ + H_2O_{aq} \rightarrow H_3O_{aq}^+ + 2 \cdot H_2O_{aq}$). While the gas-phase charged species are always allowed to enter the liquid region, liquid-phase ions are not allowed to exit from the liquid. Electrons entering the liquid solvate by reaction with $H_2O_{aq}$, described as formation of $H_2O\text{-}e_{aq}^-$. This species represents a polar water molecule strongly interacting with a free electron within the liquid bulk. The solvated electrons then undergo their own set of reactions as described in [42]. These reactions are primarily charge exchange.

Transport of gas and liquid phase species within their respective phases is given by their diffusion (or drift-diffusion) fluxes using transport coefficients for that phase. The flux of a gas phase species into the liquid, $\Gamma_{gl}$, is limited by Henry's law equilibrium at the surface of the liquid. Consider the gas phase species having density $n_g$ at the numerical node

adjacent to and $\Delta x$ away from the liquid with gas phase diffusion coefficient $D_g$. The solvated liquid phase partner has density $n_l$ at the surface of the liquid with Henry's law equilibrium constant $h$. The gas phase flux entering the liquid is,

$$\Gamma_{gl} = \frac{D_g}{\Delta x}\left(1 - \frac{n_l}{n_g h}\right)(n_g - n_l), \quad n_l \leqslant n_g h$$
$$= 0, \quad n_l > n_g h. \qquad (9)$$

The mesh spacing near the surface of the droplet is about 1 $\mu$m. The gas phase flux solvating into the liquid goes to zero when the solvated species at the surface is saturated. This limit does not mean that the entire liquid is saturated—the limit is enforced based on the saturation of the surface layer of the liquid. The flux of a liquid phase species leaving the liquid into the gas, $\Gamma_{lg}$ having diffusion coefficient in the liquid $D_l$ is:

$$\Gamma_{lg} = \frac{D_l}{\Delta x}\left(1 - \frac{n_g}{(n_l/h)}\right)(n_l - n_g), \quad n_g \leqslant \left(n_l / h\right)$$
$$= 0, \quad n_g > \left(n_l / h\right). \qquad (10)$$

The flux of species leaving the liquid goes to zero when the gas phase is saturated with respect to the liquid concentration at the surface. Again, this does not mean that the entire gas phase is saturated—the limit is based on saturation of the gas immediately adjacent to the liquid.

The use of Henry's law in in this system has certain shortcomings, even if applied only at the surface. First, Henry's law assumes the system is at kinetic equilibrium, which can result in errors for species which rapidly react upon solvating or adsorbing. Assuming kinetic equilibrium could lead to underestimating the flux of species entering the liquid [54]. However, because Henry's law is applied only at the surface, the assumed equilibrium is only local and not global. Furthermore, the limits on transport into-and-out of the liquid reflect the evolution of the species densities in time, including changes due to kinetics. At these time and length scales, the assumptions of local kinetic equilibrium hold, and Henry's law allows for first-order approximation of evolutions of densities.

The use of Henry's law also assumes thermodynamic equilibrium where it is applied, in this case only at the surface of the liquid [55]. The variations in Henry's law constants with gas temperatures can be large, changing by as much a factor of two for a 10 K change in temperature [54]. Although gas and liquid temperatures are computed, the temperature dependence of Henry's law constants is not currently accounted for in the model, which could lead to quantitative errors in the saturation densities. However, the scope of this work is to show the differences in behavior of species with vastly different $h$ values. This qualitative comparison should not be impacted by temperature because Henry's law constants for all species generally follow similar trends, increasing with temperature [56].

Rates of solvation may also vary with the radius of the droplet, particularly as the droplet evaporates. The evaporation of the microscopic droplets, particularly at low pressures and high temperatures is a complex process [57]. Evaporation initiates additional phenomena; for example, Stefan flow, wherein spatial gradients in vapor densities near the droplet cause convective movement of the fluid [58]. Proper resolution of

J. Phys. D: Appl. Phys. **52** (2019) 355207

J Kruszelnicki *et al*

Stefan flow should be addressed by dedicated models, adding a level of complexity beyond the scope of this study [59]. Here, evaporation from the liquid water into the gas is addressed by maintaining a surface density of water vapor equal to the vapor pressure of liquid water. This surface density of gas phase water then acts as a source for diffusion of water vapor into the gas. Due to limitations in the numerical mesh (the mesh is not adaptive), the volume of water is held constant.

Numerous studies have been performed in the area of atmospheric aerosols and their ability to scavenge compounds. For example, Djikaev and Tabazadeh modeled a droplet's ability to adsorb and solvate organic species as a function of the droplet diameter [60]. Their theory predicted large increases in the effective Henry's law constant for small droplets. The model requires an affinity parameter, $b$, that is related to the probabilities of adsorption and desorption which can be calculated from molecular dynamics simulations [61]. Based on these results, $b = 1.01$ for $O_3$ and $b = 11.1$ for $H_2O_2$. Using the theoretical formulation of Djikaev and Tabazadeh for the conditions in this paper, the effective $h$ increases by no more than 50% for $O_3$ and 5% for $H_2O_2$ for the smallest droplet diameter included in this study (0.1 $\mu$m). These enhancements in $h$ are small compared to the variation in Henry's law constants between species, which span 7 orders of magnitude.

To address reaction kinetics over long inter-pulse and afterglow periods, a neutral plasma option was developed for *non-PDPSIM*. Using this option, Poisson's equation is not solved and charge neutrality is enforced. The neutral-plasma option is typically invoked sufficiently after the discharge pulse that ion densities have decreased to the point that reactivity is dominated by neutral species. Any space charge that may remain at that time is removed by scaling the local densities of positive ions to match the densities of the negative ions in the regions of negative space-charge, and by increasing electron density into the regions of positive space-charge. The diffusion coefficients of all ions are then averaged to prevent charge separation and the electron density is set equal to the positive ion minus the negative ion densities. The shortest time-scales are then dictated by the reaction mechanism which then enables time-steps up to microseconds. The integration of the continuity equations in the neutral-plasma period was performed implicitly, with gradual, dynamic increases in the time-steps from $10^{-9}$ s at the end of the discharge pulse to $10^{-6}$ s towards the end of the subsequent afterglow.

Multiple discharge pulses are addressed in the same manner as described in [49]. Following simulation of the first discharge pulse during which Poisson's equation is solved, the source functions for radicals and ions are recorded. On the time scales of the inter-pulse period, the discharge pulses appear to be instantaneous. Assuming this delta-function-like production of reactive species is the same on each pulse following the first, the recorded source functions are added to the rate equations at the specified pulse repetition frequency (PRF). This integration of transport equations with impulsive additions is performed using the neutral-plasma option. This technique does not capture the change in source functions that may result from changes in gas phase densities,
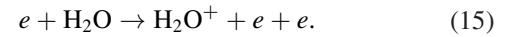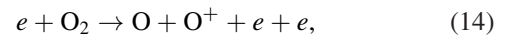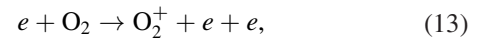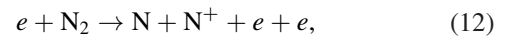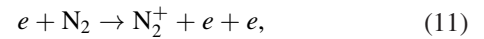
which would require that each discharge pulse be individually resolved solving Poisson's equation. It does, however, allow for approximation of source functions that enable simulation of tens to thousands of pulses, which would otherwise be prohibitive.

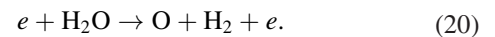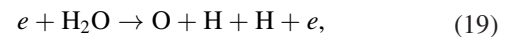## 3. Reaction mechanism, geometry and initial conditions
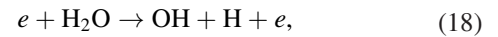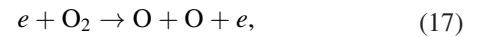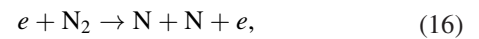
### 3.1. Reaction mechanism

This investigation addresses humid air plasma activation of liquid water droplets. The reaction mechanism is the same for the global and 2D models. The mechanism includes 88 gas phase species, 93 liquid species, 1855 gas phase reactions, and 176 liquid reactions. The electron impact rate coefficients are based on cross sections and solutions of Boltzmann's equation for the electron energy distribution in each of the models. *Pumpkin*, a reaction pathway analysis tool, was used to determine the dominant reactions producing a species of interest [62].

In the gas phase during the discharge pulse, the generation of electrons is driven by electron impact ionization of $N_2$, $O_2$, and $H_2O$ including the reactions

$$e + N_2 \rightarrow N_2^+ + e + e, \tag{11}$$

$$e + N_2 \rightarrow N + N^+ + e + e, \tag{12}$$

$$e + O_2 \rightarrow O_2^+ + e + e, \tag{13}$$

$$e + O_2 \rightarrow O + O^+ + e + e, \tag{14}$$

$$e + H_2O \rightarrow H_2O^+ + e + e. \tag{15}$$

The dominant mode of electron energy loss is inelastic collisions producing electronic, vibrational, or rotational excitation. In this reaction mechanism, the rotational and vibrational states of $O_2$ and $N_2$ are each approximated as a single state ($O_2(r)$, $O_2(v)$, $N_2(r)$, and $N_2(v)$), and only a single vibrational excited state of $H_2O$ ($H_2O(v)$) is included.

The dissociation of $O_2$, $N_2$, and $H_2O$ is critical for generating the RONS that activate water. Electron impact dissociation generates reactive products while the electron temperature is elevated during the voltage pulse, including

$$e + N_2 \rightarrow N + N + e, \tag{16}$$

$$e + O_2 \rightarrow O + O + e, \tag{17}$$

$$e + H_2O \rightarrow OH + H + e, \tag{18}$$

$$e + H_2O \rightarrow O + H + H + e, \tag{19}$$

$$e + H_2O \rightarrow O + H_2 + e. \tag{20}$$

Attachment to $O_2$ and $H_2O$ result in electron losses during and immediately after the plasma pulse, with the dissociative processes producing additional radicals,
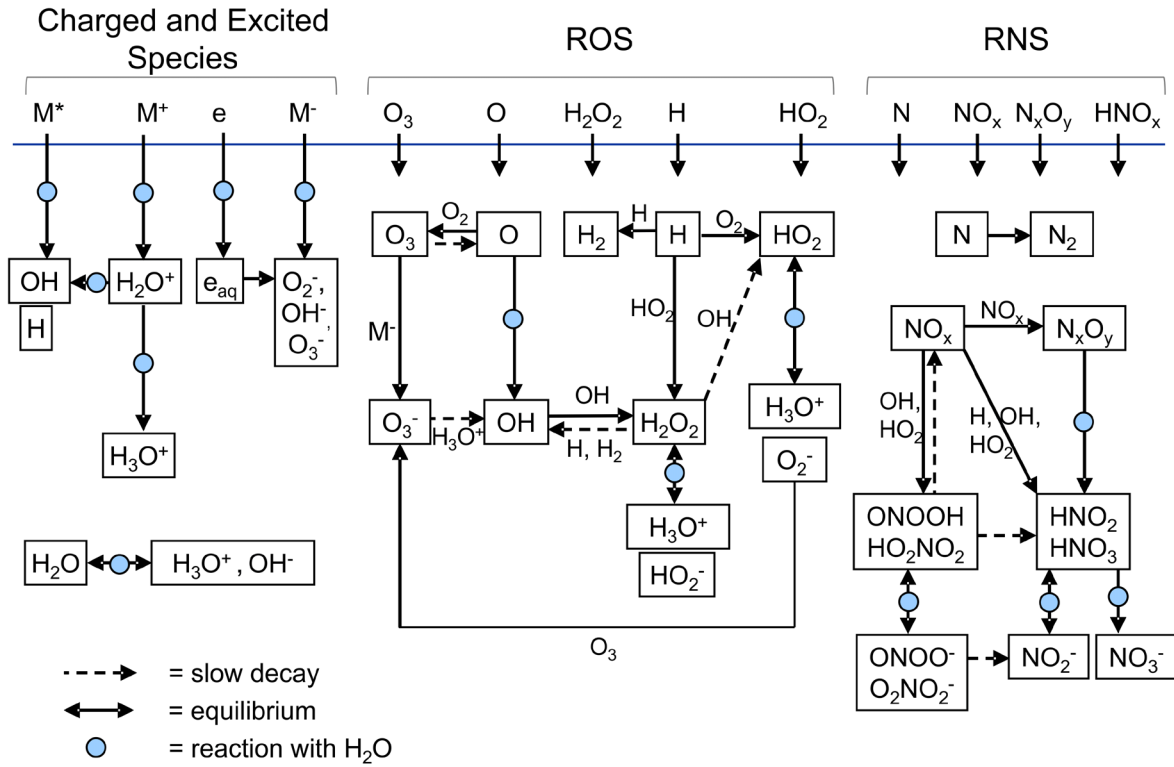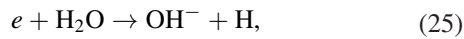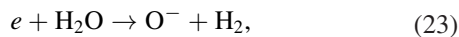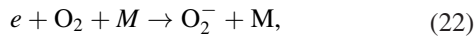
$$e + O_2 \rightarrow O + O^-, \tag{21}$$
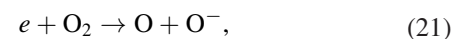
**Figure 1.** Schematic of the liquid reaction mechanism used in this investigation highlighting the most important reactions.

$$e + O_2 + M \rightarrow O_2^- + M, \tag{22}$$

$$e + H_2O \rightarrow O^- + H_2, \tag{23}$$

$$e + H_2O \rightarrow OH + H^-, \tag{24}$$

$$e + H_2O \rightarrow OH^- + H, \tag{25}$$

where M is a third body. After initial dissociation produces reactive neutrals, reactions among these species generate more complex species such as $O_3$, $H_2O_2$, $NO_x$, and $HNO_x$, through pathways that will be discussed in section 4.

The gas-phase reaction set is a modified version of the mechanism developed by Van Gaens *et al* [63]. A schematic of the liquid water reaction mechanism is in figure 1. The mechanism has been previously discussed in detail and so will only be summarized here [42]. The plasma produced species that come in contact with the liquid include electrons, positive and negative ions, excited neutrals, and ground state neutrals. The electrons that enter the liquid are rapidly solvated, and then undergo dissociative attachment with water, forming $H_{aq}$ and $OH_{aq}^-$. Most of the positive ions (with the exception of $H_3O^+$) which solvate charge exchange with $H_2O_{aq}$, forming $H_2O_{aq}^+$, followed by

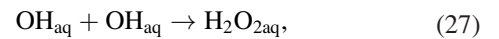$$H_2O_{aq}^+ + H_2O_{aq} \rightarrow H_3O_{aq}^+ + OH_{aq}, \tag{26}$$
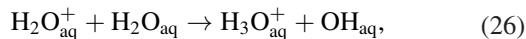
producing hydronium and a hydroxyl radical. Electronically excited gas phase species entering the liquid that have enough energy to dissociate a water molecule are assumed to produce a dissociative excitation transfer reaction with $H_2O_{aq}$ producing $H_{aq}$ and $OH_{aq}$. Excited states with less energy than
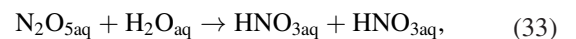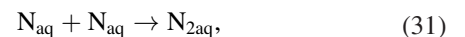
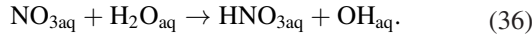this threshold energy, such as vibrationally excited molecules, simply collisionally de-excite.

The mechanism includes forward and reverse reactions for acids in the liquid, $HA_{aq}$, which enable them to dissociate and recombine according to their equilibrium pKa ($HA_{aq} + H_2O_{aq} \leftrightarrow A_{aq}^- + H_3O_{aq}^+$). These acids include $HNO_{3aq}$, $HNO_{2aq}$, $ONOOH_{aq}$, $HO_2NO_{2aq}$, $H_2O_{2aq}$, and $HO_{2aq}$. $HNO_{3aq}$ is the only strong acid which completely dissociates into $NO_{3aq}^-$ and $H_3O_{aq}^+$. During the afterglow following repetitive discharge pulses, the other weak acids stay predominately in the form of $HA_{aq}$ rather than as their conjugate bases, $A_{aq}^-$.

The reactive neutrals in the liquid are primarily produced by solvation of their gas phase counterparts. Important reactions occurring in the liquid which convert solvated species from the plasma into more stable compounds include the reactive oxygen species (ROS) reactions,
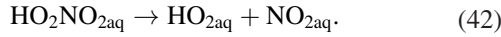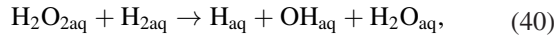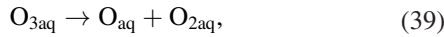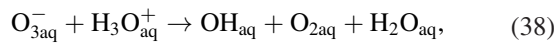
$$OH_{aq} + OH_{aq} \rightarrow H_2O_{2aq}, \tag{27}$$

$$H_{aq} + H_{aq} \rightarrow H_{2aq}, \tag{28}$$

$$O_{aq} + H_2O_{aq} \rightarrow OH_{aq} + OH_{aq}, \tag{29}$$

$$O_{aq} + O_{2aq} \rightarrow O_{3aq}, \tag{30}$$
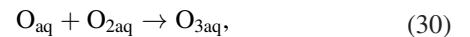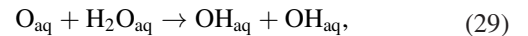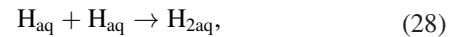
and the reactive nitrogen species (RNS) reactions,

$$N_{aq} + N_{aq} \rightarrow N_{2aq}, \tag{31}$$

$$N_2O_{5aq} \rightarrow NO_{2aq} + NO_{3aq}, \tag{32}$$

$$N_2O_{5aq} + H_2O_{aq} \rightarrow HNO_{3aq} + HNO_{3aq}, \tag{33}$$

$$N_2O_{5aq} + H_2O_{aq} \rightarrow ONOOH_{aq} + ONOOH_{aq}, \quad (34)$$

$$NO_{2aq} + OH_{aq} \rightarrow HNO_{3aq}, \quad (35)$$

$$NO_{3aq} + H_2O_{aq} \rightarrow HNO_{3aq} + OH_{aq}. \quad (36)$$

The mechanism includes slow-decay processes. Several species, including $O_{3aq}$, $H_2O_{2aq}$, $ONOOH_{aq}$, and $HO_2NO_{2aq}$ are relatively stable and often survive for several minutes after the plasma treatment. However as slow reactions or thermal decay occur at long timescales, these relatively stable species can produce more reactive products, such as $OH_{aq}$, $NO_{aq}$, $HO_{2aq}$, $O_{aq}$, and $NO_{2aq}$. These chain reactions enable plasma activated liquids to deliver reactivity long after the plasma treatment has ended. Several important slow-decay reactions include

$$H_2O_{2aq} + OH_{aq} \rightarrow HO_{2aq} + H_2O_{aq}, \quad (37)$$

$$O_{3aq}^- + H_3O_{aq}^+ \rightarrow OH_{aq} + O_{2aq} + H_2O_{aq}, \quad (38)$$

$$O_{3aq} \rightarrow O_{aq} + O_{2aq}, \quad (39)$$

$$H_2O_{2aq} + H_{aq} \rightarrow H_{aq} + OH_{aq} + H_2O_{aq}, \quad (40)$$

$$ONOOH_{aq} + H_2O_{aq} \rightarrow OH_{aq} + NO_{2aq} + H_2O_{aq}, \quad (41)$$

$$HO_2NO_{2aq} \rightarrow HO_{2aq} + NO_{2aq}. \quad (42)$$

Although the reaction mechanisms are the same, there are differences in handling the species between the global and 2D models. For purposes of accounting, the global model requires an equivalent liquid species for every gas phase species (e.g. OH and $OH_{aq}$). When, for example, gas phase OH diffuses to the interface, solvates and appears in the liquid, the density of OH in the gas zone is decreased and the density of $OH_{aq}$ in the liquid phase is increased. This method of duplicate species is necessary in the global model to track if a species in the gas or liquid. In the 2D model, a species is a gas phase or solvated species depending on its location in the mesh—gas phase or liquid. In cases where different reactions occur in the gas and liquid phases for the same gas phase and solvated analogues, the same radical is treated as a different species in the gas and liquid. In doing so, an artificial reaction was added to the mechanism to quickly convert a gas species to its solvated analogue (or vice versa) when crossing the gas–liquid interface. With prior knowledge of the importance or lifetimes of a species, the gas-to-liquid conversion can be used to economize on the number of species and reactions. For example, knowing that $N_2(v)$ quickly collisionally relaxes as it solvates into the water, a single reaction was used to represent both processes, $N_2(v) + H_2O_{aq} \rightarrow N_{2aq} + H_2O_{aq}$. Using this method, the number of liquid species in the 2D model was reduced from 93 to 36 without significantly changing the reaction mechanism.

In the discussion that follows, particular attention will be paid to ozone and hydrogen peroxide due to the large difference in their Henry's law constants ($\approx 0.274$ and $\approx 1.92 \times 10^6$, respectively), their stability in aqueous form, and their use in biological processes and abatement of pollutants. The

hydroxyl radical will also be discussed due to its high reactivity. Note will also be made of the pH of the droplets. The pH of the droplets was calculated based on the molarity of hydronium, $H_3O_{aq}^+$,

$$pH = -\log_{10}\left(\frac{[H_3O_{aq}^+]}{N_A}\right), \quad (43)$$

where the density of $H_3O_{aq}^+$ is in molecules/liter, and $N_A$ is Avogadro's number.

### 3.2. Global model parameters

The base case geometry for the global model is a cylinder with a radius of 2.5 mm and a height of 2 mm containing one 10 $\mu$m droplet of water at its center. This geometry corresponds to a plasma volume of 39.3 mm$^3$, a plasma surface area of 39.3 mm$^2$ (when reactions are ignored on the outer walls), a liquid volume of 523 $\mu$m$^3$, and a liquid surface area of 314 $\mu$m$^2$, or a SVR of 600/cm. In cases with a single droplet, the diffusion length was defined as the $d/\pi$, where $d$ is the distance between the droplet surface and the top or bottom surfaces of the cylinder. The diffusion length was 317 $\mu$m for the base case. The radial surface was not considered a wall for loss processes, which then represents a periodic boundary condition, or an infinite planar DBD. No convective gas flow was considered. The gas phase initially consists of $N_2/O_2/H_2O/CO_2 = 76.6/20.3/3.52/0.03$ at 1 atm and 300 K. The water initially contains dissolved gases with concentrations of $N_{2aq}$ (8.9 ppm), $O_{2aq}$ (4.8 ppm), and $CO_{2aq}$ (0.14 ppm). The pulse repetition rate of the discharge was 10 kHz. The discharge was simulated for 500 pulses followed by an afterglow bringing the total simulation time to 10 s. During the afterglow, the discharge is not pulsed but otherwise the full reaction mechanism is employed.

### 3.3. 2D model parameters

Two types of 2D simulations were performed to distinguish the effects of the non-uniformity of the plasma from the spatial dependence of solvation of reactive species. The first simulation, called *reactive diffusion*, addresses a single water droplet surrounded by humid air containing a uniform density of RONS. The simulation tracks the resulting transport and chemistry as these species react in the gas phase, solvate and react in the water. The second type of simulation is of a DBD in which an ionization wave (IW) of a single plasma filament produces a non-uniform distribution of RONS.

A schematic of the reactive diffusion geometry is in figure 2. The numerical mesh is cylindrically symmetric about the left boundary with a single water droplet at the center. The initial densities of gas-phase species were taken from global modeling after 500 pulses with no liquid present in the reactor, but otherwise with parameters the same as the base case. These initial densities are in table 2. The liquid was initialized with a pH = 7 (1.85 ppb $H_3O_{aq}^+$ and $OH_{aq}^-$), and with the Henry's law equilibrium density of $N_{2aq}$ (8.75 ppm) and $O_{2aq}$ (4.69 ppm).

J. Phys. D: Appl. Phys. **52** (2019) 355207
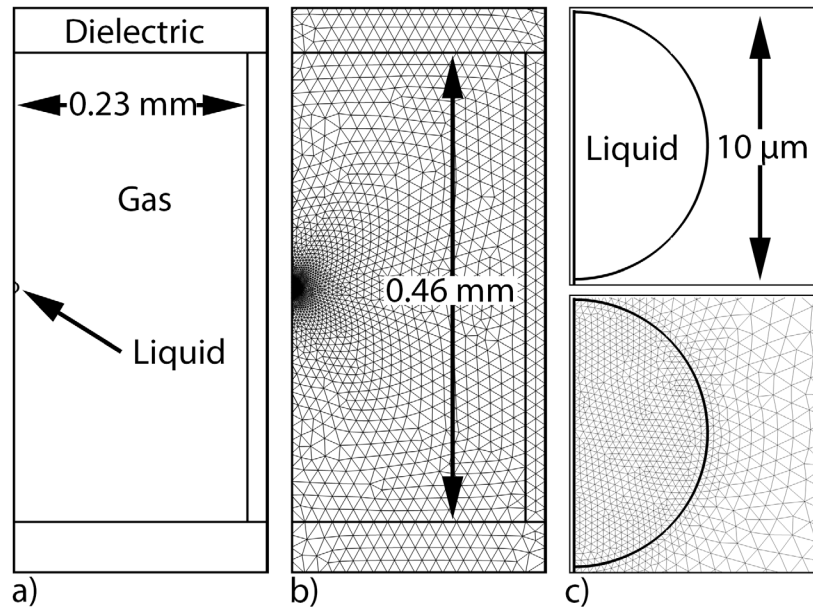
J Kruszelnicki *et al*



**Figure 2.** Numerical parameters for the base case of a droplet initially exposed to a uniform density of plasma activated species. The sizes of the droplet and reactor were varied to maintain a constant liquid/gas ratio. (a) Geometry, (b) numerical mesh and (c) close-up of droplet.

**Table 2.** Initial gas phase densities for 2D reaction diffusion simulations.

| Species[a] | Density (cm$^{-3}$) | Species | Density (cm$^{-3}$) |
|---|---|---|---|
| $N_2$ | $1.87 \times 10^{19}$ | $HO_2NO_2$ | $5.95 \times 10^{12}$ |
| $O_2$ | $4.92 \times 10^{18}$ | $NO_3$ | $4.35 \times 10^{11}$ |
| $H_2O$ | $8.58 \times 10^{17}$ | $H$ | $1.65 \times 10^{10}$ |
| $O_3$ | $2.07 \times 10^{16}$ | $O_2(^1\Sigma_u)$ | $3.95 \times 10^{9}$ |
| $O_2(^1\Delta_g)$ | $5.09 \times 10^{14}$ | $N_2O_4$ | $1.42 \times 10^{8}$ |
| $HNO_3$ | $2.54 \times 10^{14}$ | $HNO$ | $1.02 \times 10^{8}$ |
| $N_2O$ | $1.52 \times 10^{14}$ | $H_3O^+(H_2O)_6$ | $1.95 \times 10^{7}$ |
| $H_2O_2$ | $1.44 \times 10^{14}$ | $NH$ | $1.06 \times 10^{7}$ |
| $HNO_2$ | $5.14 \times 10^{13}$ | $O_2^-(H_2O)_2$ | $9.44 \times 10^{6}$ |
| $O$ | $1.98 \times 10^{13}$ | $OH^-(H_2O)_2$ | $7.22 \times 10^{6}$ |
| $H_2$ | $3.67 \times 10^{13}$ | $e^-$ | $1.05 \times 10^{6}$ |
| $NO_2$ | $2.46 \times 10^{13}$ | $O_2^-$ | $2.85 \times 10^{5}$ |
| $N_2O_5$ | $1.49 \times 10^{13}$ | $NO_2^+$ | $1.53 \times 10^{5}$ |
| $NO$ | $1.39 \times 10^{13}$ | $O_3^-$ | $1.55 \times 10^{5}$ |
| $OH$ | $1.37 \times 10^{13}$ | $NO_2^-$ | $1.53 \times 10^{5}$ |
| $N$ | $8.91 \times 10^{12}$ | $OH^-$ | $4.48 \times 10^{4}$ |
| $HO_2$ | $6.90 \times 10^{12}$ | | |

[a] Species are sorted in order of decreasing density.

Electrodynamic equations were not solved in this geometry with the intent of investigating space-resolved droplet chemistry in a reactor following many discharge pulses, but without direct plasma interaction with the liquid.

The second geometry shown in figure 3 is that of a DBD reactor with a 1 mm gas gap and, for the base case, a $d = 10$ $\mu$m diameter liquid droplet at its center. The mesh was cylindrically symmetric about the left boundary. The resolution of the mesh varied from 90 $\mu$m in the bounding solids to 1 $\mu$m near the surface of the droplet. The mesh nodes neighboring the surface of the liquid were equidistant from the surface to prevent artificial enhancement of electric fields and solvation
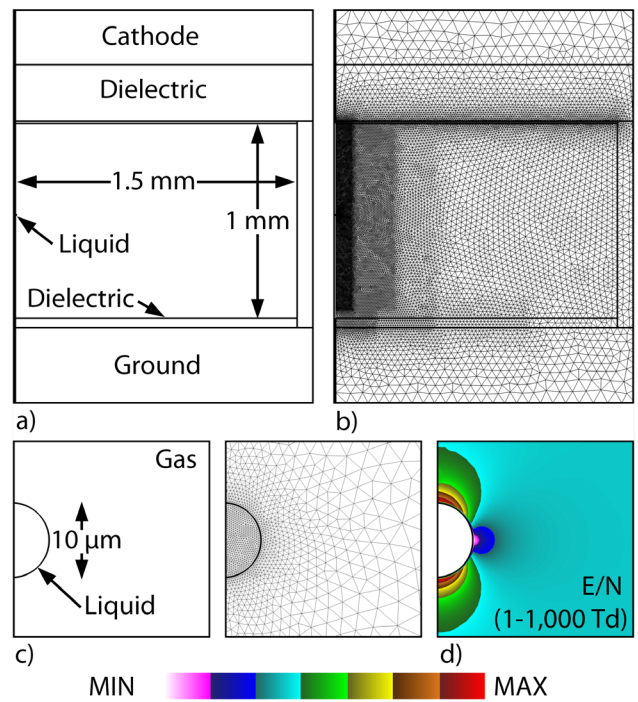


**Figure 3.** Set-up for simulation of a single-filament DBD discharge activating a single water droplet. (a) Reactor geometry, (b) numerical mesh (c) enlargement of volume and mesh around the droplet, and (d) initial *E/N* (1 Td = $10^{-17}$ V cm$^2$) near the droplet. The size of the droplet was varied.

rates. The top electrode is the cathode while the bottom electrode is grounded. Both electrodes were covered by a dielectric with $\varepsilon/\varepsilon_0 = 4.0$. A small cloud of neutral plasma (electrons and oxygen and nitrogen ions) was initialized at the intersection of the axis and the top dielectric to launch a single plasma filament. The peak density was $10^{11}$ cm$^{-3}$, with a Gaussian distribution to $10^6$ cm$^{-3}$, resulting in a radius of

J. Phys. D: Appl. Phys. **52** (2019) 355207

J Kruszelnicki *et al*

approximately 50 $\mu$m. No other pre-ionization was included. The gas was humid air having a relative humidity of 29% ($N_2$/$O_2$/$H_2O$ = 78/21/1). As in the reactive diffusion simulations, the water was initialized as being at equilibrium with air with $N_{2aq}$ and $O_{2aq}$ at their Henry's law equilibrium densities, and a pH $\approx$ 7. This geometry is intended to represent the worst-case of a non-uniform discharge to emphasize the importance of de-solvating reactions, as discussed below.

## 4. Global modeling of plasma activated droplets

### 4.1. Base case

When using the global model, each discharge pulse is simulated in full detail, with conditions prior to the pulse being initialized with a minimum electron density of $n_e = 10^8$ cm$^{-3}$ and an electron temperature of $T_e = 0.025$ eV. The first discharge pulse and plasma properties are shown in figure 4(a). As the power begins to increase, $T_e$ increases to a maximum of 6.4 eV. As the gas begins to avalanche, increasing the plasma density and increasing conductivity, the power is dissipated by a larger number of electrons, resulting in a lower $T_e$. The volume averaged electron density reaches $1.8 \times 10^{11}$ cm$^{-3}$ near the peak power of 1 kW or 25.4 kW cm$^{-3}$. The energy deposition is 5 $\mu$J/pulse (127 $\mu$J cm$^{-3}$) or an average power of 50 mW (1.27 W cm$^{-3}$) at 10 kHz. The energy deposition corresponds to 0.016 eV per gas molecule over 500 pulses.
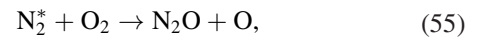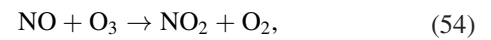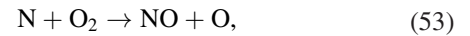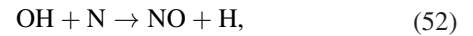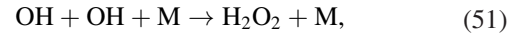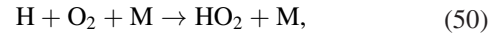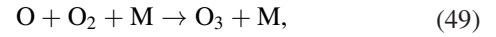
Attachment dominates in the afterglow, producing an ion-ion plasma prior to the next discharge pulse (figures 4(b) and (c)). The dominant ions in this afterglow are $H_3O^+(H_2O)_n$, and $O_2^-(H_2O)_n$, $O^-(H_2O)$, and $OH^-$. The dominance of water cluster ions begins during the discharge pulse, becoming the most abundant positive ion by 6 ns. The most abundant cluster ion is $H_3O^+(H_2O)_6$, which is the largest water cluster ion included in the reaction mechanism. The density of $H_3O^+(H_2O)_6$ reaches a maximum of $4 \times 10^{11}$ cm$^{-3}$ 20 ns after the start of the pulse and decays by ion-ion recombination to $2 \times 10^{10}$ cm$^{-3}$ before the start of the next discharge pulse.

Electron impact dissociation of water during the discharge pulse produces OH, H, and $H_2$, dissociation of $O_2$ produces O, and dissociation of $N_2$ produces N. These species also continue to be produced for approximately 10 $\mu$s after each pulse by the cascade of reactions that results from charge exchange, recombination, and electronic excitation. For example, the reactions

$$N_2^* + O_2 \rightarrow N_2 + O + O, \tag{44}$$

$$O^-(H_2O) + H_2O \rightarrow OH^-(H_2O) + OH, \tag{45}$$

$$OH^-(H_2O)_n + H_3O^+(H_2O)_n \rightarrow H + OH + (H_2O)_n, \tag{46}$$

$$H_2NO^+ + M^-(H_2O)_n \rightarrow N + M + (H_2O)_n, \tag{47}$$

$$O^+ + N_2 + M \rightarrow NO^+ + N + M, \tag{48}$$
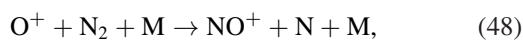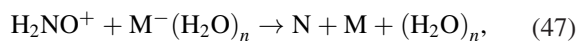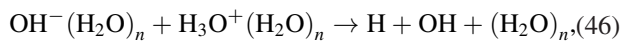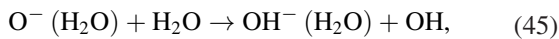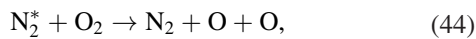
continue to produce reactive species as long as 10 $\mu$s into the afterglow. The electrons undergo rapid attachment in the afterglow, with densities that decrease an order of magnitude

within 20 ns. As a result, dissociative recombination of electrons (e.g. $e + O_2^+ \rightarrow O + O$) does not significantly contribute to the production of OH, O, and N. (In contrast, in prior studies of He atmospheric pressure plasma jets with air impurities, dissociative recombination of impurity ions [$O_2^+$, $N_2^+$, $H_2O^+$] were found to be major sources of O, N and OH radicals in the afterglow [64].) The dissociation products then react with other RONS and the surrounding air, for example,

$$O + O_2 + M \rightarrow O_3 + M, \tag{49}$$

$$H + O_2 + M \rightarrow HO_2 + M, \tag{50}$$

$$OH + OH + M \rightarrow H_2O_2 + M, \tag{51}$$

$$OH + N \rightarrow NO + H, \tag{52}$$

$$N + O_2 \rightarrow NO + O, \tag{53}$$

$$NO + O_3 \rightarrow NO_2 + O_2, \tag{54}$$

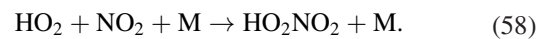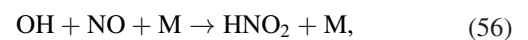$$N_2^* + O_2 \rightarrow N_2O + O, \tag{55}$$

where M is a third body.

The evolution of gas phase RONS during the first 10 discharge pulses is shown in figures 5(a) and (b). These species can be grouped based on their lifetimes. Several of the most reactive species (e.g. $O_2(^1\Sigma)$, $O(^1D)$, $N_2^*$, and $OH(A^2\Sigma)$) are depleted by chemical reactions or collisional relaxation before the beginning of the next pulse, and are not shown in the figure. (These species would appear to be delta-functions in the figure.) Even though the lifetimes of these species may be short, they nevertheless can make important contributions to radical production. For example, dissociative excitation transfer of $N_2^*$ to $O_2$ produces 56% of the O atoms by 20 ns after the discharge pulse, with the rest being produced by electron impact dissociation of $O_2$. The next group of species reaches a pulsed periodic steady-state, where they are produced during the discharge pulse and partly consumed between pulses. Species in this group include O, OH, and $HO_2$. The density of O atoms reaches $3 \times 10^{13}$ cm$^{-3}$ 100 ns after the start of the pulse, and is reduced by a factor of nearly 100 by the formation of $O_3$ (equation (49)) before the next pulse. The densities of OH (with a maximum of $1.5 \times 10^{13}$ cm$^{-3}$) and $HO_2$ ($3.5 \times 10^{13}$ cm$^{-3}$) are not as significantly depleted between the pulses, with the densities decreasing only 10-50% before the next pulse.

Lastly, there are species which accumulate from pulse to pulse or whose densities come into a steady state over many pulses, summarized in figure 5(c). ROS which accumulate over the 500 pulses (and their maximum densities) include $O_3$ ($1 \times 10^{16}$ cm$^{-3}$), $H_2O_2$ ($1 \times 10^{14}$ cm$^{-3}$), and $H_2$ ($2 \times 10^{13}$ cm$^{-3}$).

The RNS further react to form higher order nitrogen oxides and acids. For example,

$$OH + NO + M \rightarrow HNO_2 + M, \tag{56}$$

$$OH + NO_2 + M \rightarrow HNO_3 + M, \tag{57}$$

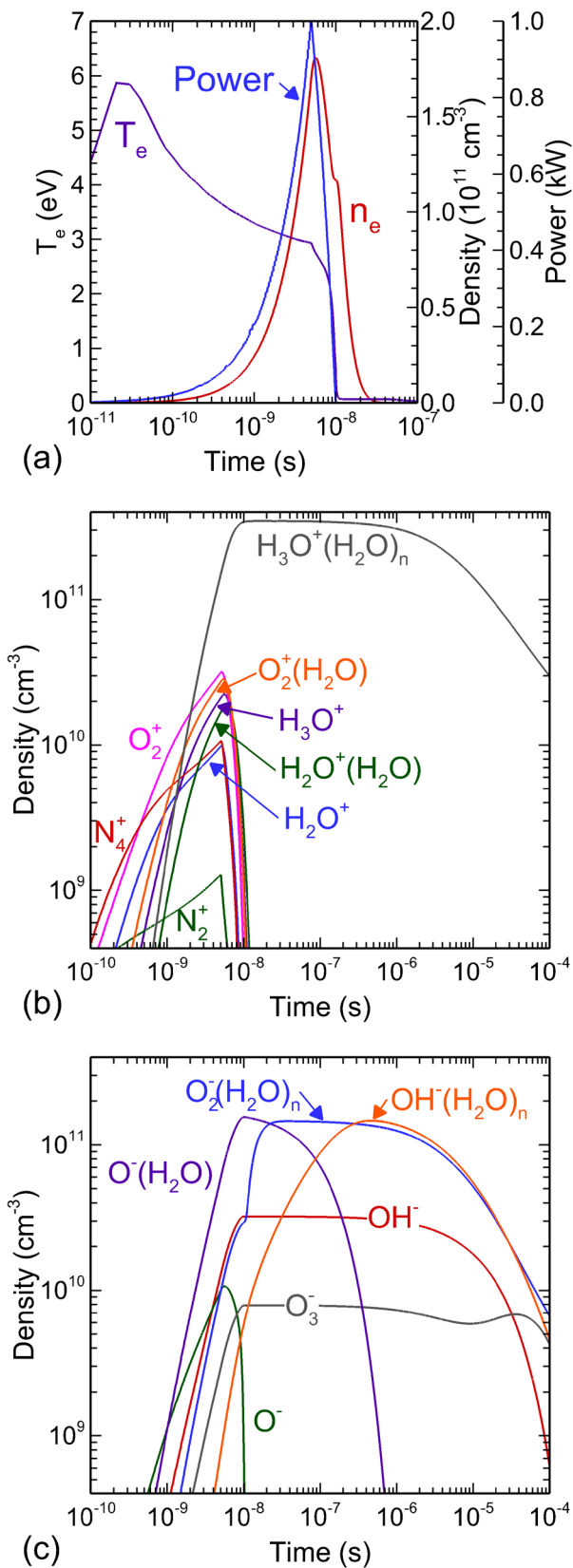$$HO_2 + NO_2 + M \rightarrow HO_2NO_2 + M. \tag{58}$$

**Figure 4.** Plasma properties of the first discharge pulse. (a) The applied power deposition at each pulse as a function of time, and the resulting electron temperature ($T_e$) and electron density ($n_e$). The power deposition is a triangular pulse with a total duration of 10 ns. (b) Positive and (c) negative ions during the first discharge pulse and afterglow.
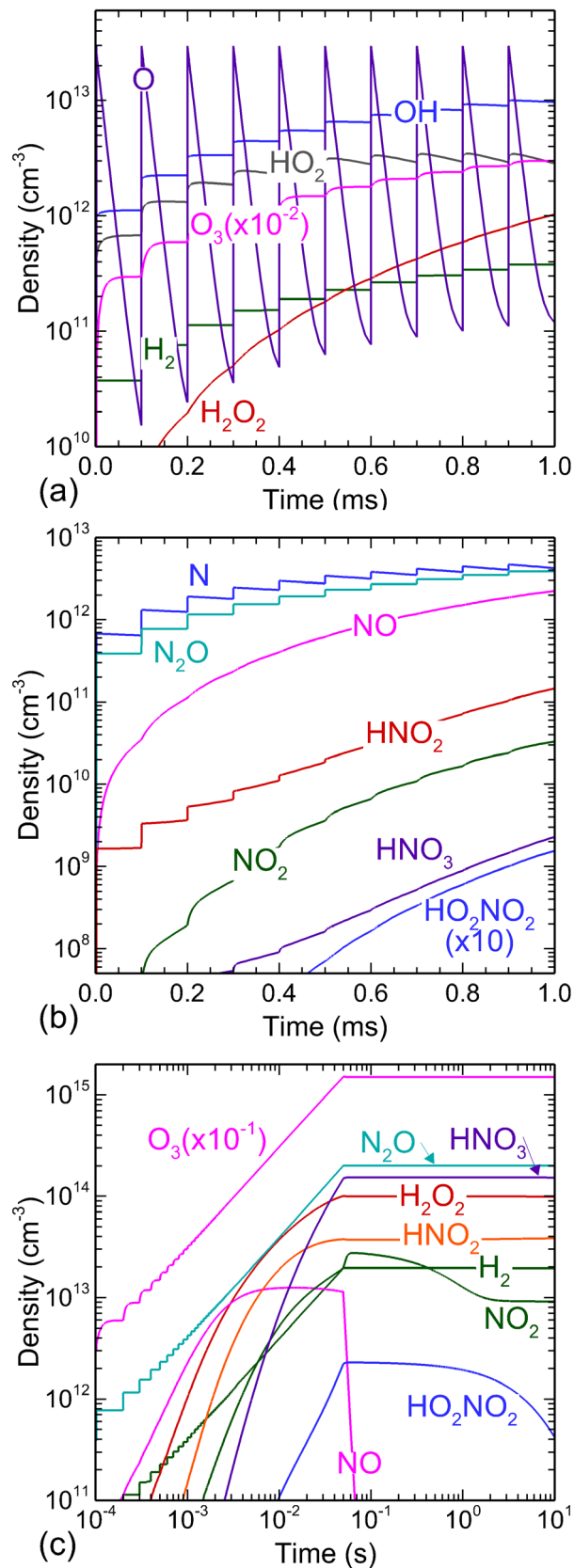
**Figure 5.** Gas phase reactive neutral species generated in a humid air discharge containing a single 10 $\mu$m droplet. (a) ROS and (b) RNS during the first 10 discharge pulses. (c) Accumulation of selected species during 500 pulses and an afterglow period.
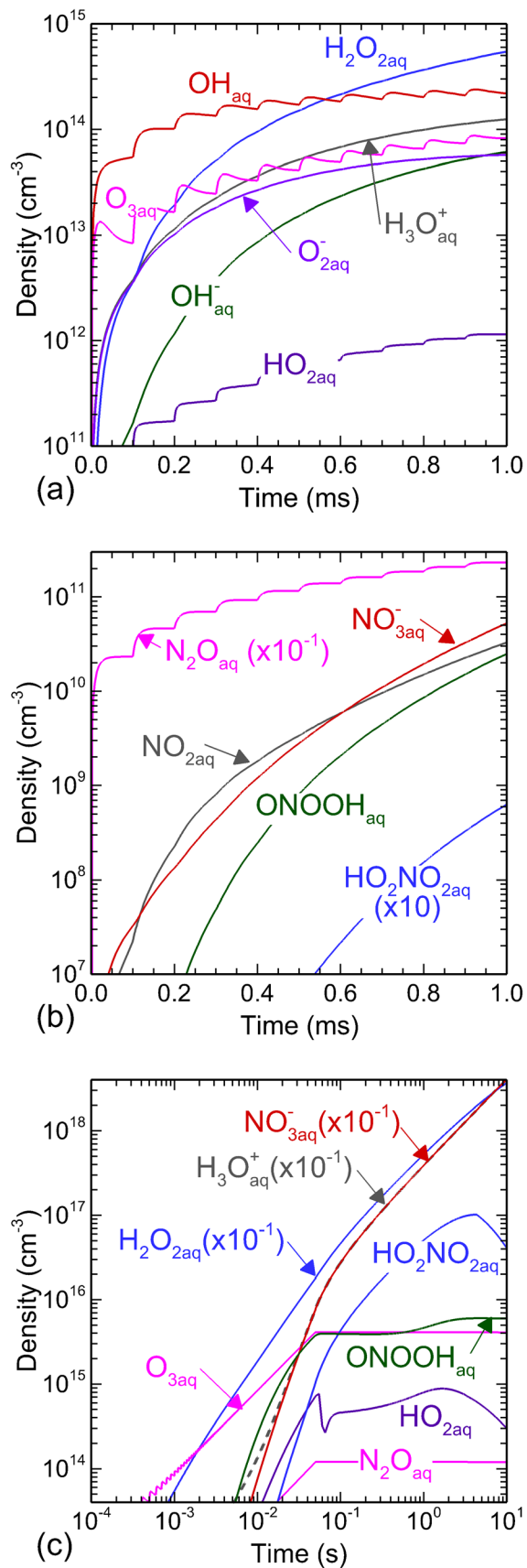
**Figure 6.** Liquid phase reactive species produced in a single 10 $\mu$m droplet in a humid air discharge. (a) ROS and (b) RNS during the first ten discharge pulses. (c) Accumulation of selected aqueous species during 500 pulses and an afterglow period.
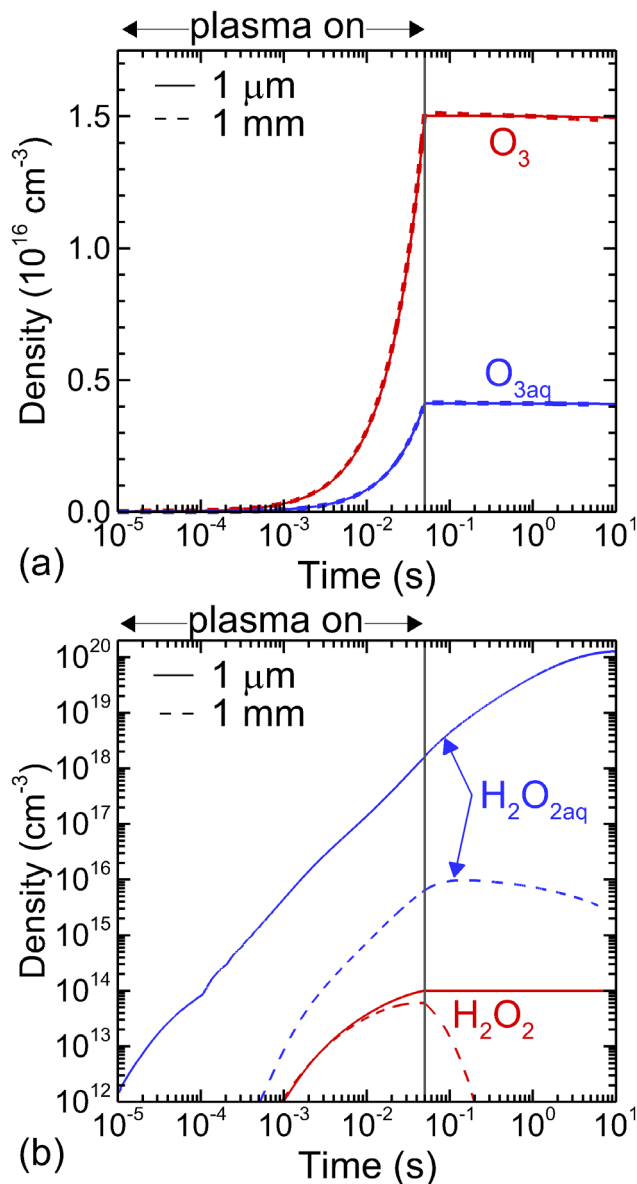


**Figure 7.** Comparison of densities for species with a low Henry's law constant $h$, $O_3$ ($h = 0.274$ and high $h$, $H_2O_2$ ($h = 1.92 \times 10^6$) for single droplets of 1 $\mu$m and 1 mm diameter as a function of time. (a) Densities of $O_3$ and $O_{3aq}$. Note that densities for both diameters are plotted, but are nearly indistinguishable. (b) Densities of $H_2O_2$ and $H_2O_{2aq}$. The liquid density differs significantly based on droplet diameter. The plasma on period, which includes 500 pulses at 10 kHz, is indicated. Note that in (a) the densities are plotted on a linear scale and in (b) the densities are plotted on a log scale.

These products generally take many steps to form, and therefore have a slower, smoother evolution in time, despite the pulsed nature of the plasma. RNS which accumulate over the 500 pulses (and their maximum densities) include $N_2O$ ($2 \times 10^{14}$ $cm^{-3}$), $HNO_3$ ($1 \times 10^{14}$ $cm^{-3}$), $HNO_2$ ($4 \times 10^{13}$ $cm^{-3}$), $NO_2$ ($2 \times 10^{13}$ $cm^{-3}$) and $HO_2NO_2$ ($2 \times 10^{12}$ $cm^{-3}$). The density of NO initially increases over many pulses, and reaches a pulsed periodic steady state after tens of pulses with a density of $1 \times 10^{13}$ $cm^{-3}$.

Densities of aqueous species during the first ten pulses of the base case (a single 10 $\mu$m diameter water droplet)

are shown in figures 6(a) and (b). The evolution of aqueous species during the 500 discharge pulses and the afterglow is shown in figure 6(c). Ions and electrons from the plasma directly solvate into the water droplet while neutrals solvate if the liquid densities are below their Henry's law saturation values. In the droplet, several charged species are stable and accumulate (e.g. $H_3O_{aq}^+$, $O_{2aq}^-$, and $NO_{3aq}^-$). $H_3O_{aq}^+$ and $NO_{3aq}^-$ are the most abundant ions, with densities of $7 \times 10^{16}$ cm$^{-3}$ ($1 \times 10^{-4}$ M, where M is moles/liter) at the end of the plasma period. $O_{2aq}^-$ reaches a density of $9 \times 10^{13}$ cm$^{-3}$ ($1 \times 10^{-7}$ M). $O_2NO_{2aq}^-$, the conjugate base of $HO_2NO_{2aq}$, reaches a density of $2 \times 10^{13}$ cm$^{-3}$ ($3 \times 10^{-8}$ M). These negative liquid ions and hydronium are to some extent due to solvation of gaseous ions, but are predominately a result of the solvation of neutral acids, followed by hydrolysis in water. With the exception of $H_3O^+$ (and its cluster ions), positive gas phase ions (e.g. $N_2^+$, $O_2^+$) rapidly charge exchange with water, followed by the hydrogen abstract reaction $H_2O_{aq}^+ + H_2O_{aq} \rightarrow H_3O_{aq}^+ + OH_{aq}$. (The ionization energy of $O_2$ is less than that of $H_2O$ in the gas phase, but in the presence of water, formation of $H_3O^+$ and OH is energetically favorable [65].) Though electronically excited states are allowed to solvate, their lifetimes are short as they undergo a collisional de-excitation in the liquid. The more stable species solvating into the water tend to build up from pulse to pulse.

$OH_{aq}$ and $H_{aq}$ are a result of electron impact reactions in the gas phase that produce OH and H, followed by their solvation, as well as excited states that enter the liquid with enough energy to dissociate water. $H_2O_{2aq}$ is a product of reactions of OH in the gas phase, followed by solvation, and by reactions of $OH_{aq}$ in liquid. $O_{3aq}^-$ results primarily from charge exchange between other aqueous negative ions and $O_{3aq}$. From pulse to pulse, the pH of the droplet decreases, becoming more acidic, with a pH of 3.9 by the end of the pulsing period. The decreasing pH is due to the production of $HNO_{3aq}$, which is a strong acid which dissociates into $H_3O_{aq}^+$ and $NO_{3aq}^-$. $HNO_{3aq}$ continues to form from solvation of $HNO_3$ for seconds after the discharge pulses terminate, and the pH is 1.25 after 10 s. There are also several weak acids produced, including $HNO_{2aq}$, $HO_{2aq}$, $HO_2NO_{2aq}$, $ONOOH_{aq}$, and $H_2O_{2aq}$.

Several of the more complex RNS were a result of reactions in the liquid. For example, $N_2O_5$ is formed in the gas phase from reactions between $NO_2$ and $NO_3$. Upon solvating into the water droplet, $N_2O_5$ is converted to $ONOOH_{aq}$ or $HNO_{3aq}$ (equations (33) and (34)). As a result $ONOOH_{aq}$ accumulates to a density of $4 \times 10^{15}$ cm$^{-3}$ ($6 \times 10^{-6}$ M) by the end of 500 pulses. $ONOOH_{aq}$ and $HO_2NO_{2aq}$ are important species for long timescale liquid activation, as they can generate more reactive species several seconds after the plasma treatment. $HO_2NO_{2aq}$ decays into $HO_{2aq}$ and $NO_{2aq}$ (equation (41)), and $ONOOH_{aq}$ decays into $OH_{aq}$ and $NO_{2aq}$ (equation (42)). $HO_2NO_{2aq}$ reaches a density of $1 \times 10^{15}$ cm$^{-3}$ ($2 \times 10^{-6}$ M) by the end of 500 pulses, and due to solvation of $HO_2NO_2$ continues to increase in the afterglow to a density of $4 \times 10^{17}$ cm$^{-3}$ ($7 \times 10^{-4}$ M).
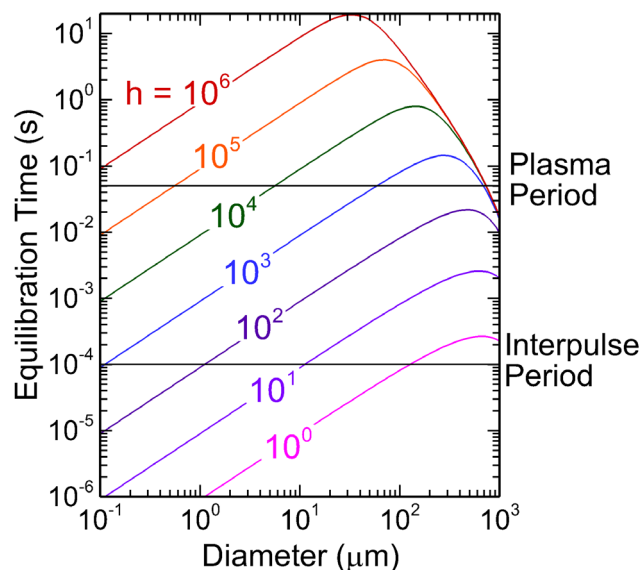


**Figure 8.** Equilibration time for solvation as a function of droplet diameter and Henry's law constant (equation (63)). The horizontal lines show the inter-pulse period and the duration of the total plasma-on period (500 pulses).

### 4.2. Droplet diameter—finite plasma volume

The range of Henry's law constants for RONS produced in air plasmas is nearly $10^7$. This large range results in significantly different activation of the liquid, leading to droplet size dependent densities of aqueous species. These trends are illustrated by the densities of $O_{3aq}$ and $H_2O_{2aq}$ in 1 $\mu$m and 1 mm droplets shown in figure 7. Densities are shown during 500 discharge pulses in humid air at 10 kHz (elapsed time of 0.05 s) followed by a 10 s afterglow. $O_3$ accumulates in the gas phase, reaching a density of $1.5 \times 10^{16}$ cm$^{-3}$ after 500 pulses. $O_3$ also has a low Henry's law constant of 0.274, which has two important implications. Given the small volume of the droplet compared to the plasma (gas to liquid volume ratios are $7.50 \times 10^7$ for a 1 $\mu$m droplet and 73.9 for a 1 mm droplet), most of the $O_3$ produced in the plasma remains in the gas phase instead of solvating into the droplet. As a result, the gaseous $O_3$ is not depleted by solvation into the droplet. Second, with such large densities of $O_3$ and large fluxes incident onto the surface of the droplet, the equilibration time for saturating the droplet with $O_{3aq}$ is shorter than the inter-pulse period. As a result, $n_l \approx hn_g$ (that is, $O_3$ and $O_{3aq}$ are at equilibrium) during the majority of the plasma treatment. The end result is that $O_3$ and $O_{3aq}$ densities were nearly independent of the diameter of the droplet.

$H_2O_2$, on the other hand, has a high Henry's law constant of $1.92 \times 10^6$. This value of $h$ is smaller than the ratio of volumes of the smaller droplet but larger than the ratio of the volumes of the larger droplet. These combinations of volume ratios and Henry's law constant implies that the smaller droplet can be saturated with $H_2O_{2aq}$ and most of the $H_2O_2$ produced in the gas phase remains in the gas phase. For the larger droplet, most of the $H_2O_2$ produced in the gas phase (which reaches a
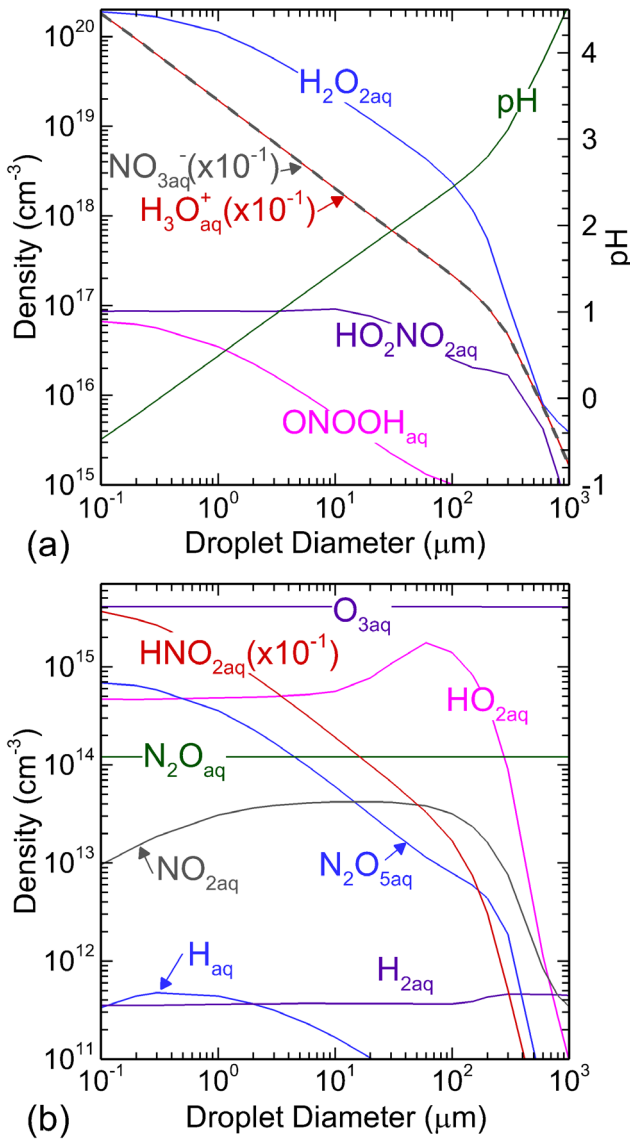
**Figure 9.** Density of liquid RONS as a function of droplet diameter for species with (a) $h \geq 10^5$ and (b) $h \leq 10^5$. The data are compared after 500 pulses and an afterglow period for a total time of 5 s. The simulation was for a single droplet.

density of $1.0 \times 10^{14}$ cm$^{-3}$) is solvated, resulting in a depletion of gas phase H$_2$O$_2$. In terms of aqueous densities, small droplets saturate (that is, H$_2$O$_2$ and H$_2$O$_{2aq}$ are at equilibrium). For the larger droplet, the same gas phase production of H$_2$O$_2$ is diluted in a larger liquid volume, resulting in the density of H$_2$O$_{2aq}$ being 4 orders of magnitude lower for the 1 mm droplet compared to the 1 $\mu$m droplet. The maximum density of H$_2$O$_{2aq}$ is $1.2 \times 10^{20}$ cm$^{-3}$ (0.2 M) in the 1 $\mu$m droplet and $9.7 \times 10^{15}$ cm$^{-3}$ ($2 \times 10^{-5}$ M) for the 1 mm droplet. The equilibration time for the 1 mm droplet is longer than the time the discharge is on, as indicated by $n_l < hn_g$ for most of the simulation time.

Varying the droplet diameter for a single droplet can have a significant impact on the activation of the liquid by species having different Henry's law constants. Consider a non-reacting species which initially entirely resides in the gas phase with an initial density, $n_{g0}$. Equilibrium of the gas phase

species with its aqueous counterpart in the droplet occurs when $n_{l\infty} = hn_{g\infty}$, where $n_{l\infty}$ and $n_{g\infty}$ are the final densities in the liquid and the gas. Ignoring other reactions, the total number of molecules in the gas phase and liquid must be conserved,

$$V_g n_{g0} = V_l n_{l\infty} + V_g n_{g\infty}, \tag{59}$$

where $V_l$ is the droplet volume and $V_g$ is the gas volume. The final equilibrium liquid density would then be

$$n_{l\infty} = \frac{h}{1 + h\frac{V_l}{V_g}} n_{g0}. \tag{60}$$

This relationship has two limiting values:

$$n_{l\infty} = hn_{g0} \quad \text{for} \quad h\frac{V_l}{V_g} \ll 1, \tag{61}$$

$$n_{l\infty} = \frac{V_g}{V_l} n_{g0} \quad \text{for} \quad h\frac{V_l}{V_g} \gg 1. \tag{62}$$

In the first case (equation (61)), the density of the solvent in the water saturates, $n_{l\infty}$ is independent of $V_l/V_g$, and so is also independent of droplet diameter. This limit applies to species with low Henry's law constants, including O$_3$, N$_2$O, and H$_2$. The end result is that the density of their aqueous partners are independent of droplet diameter. In the second case (equation (62)), the majority of the molecules that started in the gas phase are solvated, and the concentration of the aqueous partner in the liquid is limited by depletion of the gas phase. This limit results in $n_{l\infty}$ being a function of $V_g/V_l$ and so is also a function of droplet diameter. This limit applies to species with a high Henry's law constant, including H$_2$O$_2$, HO$_2$NO$_2$, and HNO$_3$.

The limits presented in equations (61) and (62) describe the steady state conditions but not the timescales to reach this equilibrium. Using the assumptions of solvation dynamics which are applied in the global model, it is possible to estimate these timescales. Based on equations (2) and (4), the equilibration time (neglecting reactions) for activating a droplet, $\tau$, is

$$\tau = \frac{\Lambda^2}{Df_l\left(\frac{V_g}{hV_l} + 1\right)}. \tag{63}$$

The derivation of $\tau$ is in the appendix. This equilibration time is plotted for $D = 0.19$ cm$^2$ s$^{-1}$ in figure 8. The equilibration time, $\tau$, initially increases with droplet diameter, as the SVR decreases, and increases with Henry's law constant. The species with the largest $h$, such as H$_2$O$_{2aq}$, are the slowest to equilibrate, which is consistent with the results shown in figure 7. Above a critical diameter, the equilibration time begins to decrease as $hV_l/V_g$ exceeds 1 and the gas phase begins to become depleted. The depletion of gas phase partners results in an equilibration time which is limited by the area of the droplet ($f_l$).

Aqueous species densities as a function of droplet diameter for a single droplet after 500 discharge pulses and an afterglow bringing the total time to 5 s are shown in figure 9. The densities of species with high Henry's law constants, H$_2$O$_{2aq}$, HO$_2$NO$_{2aq}$, NO$_{3aq}^-$, and ONOOH$_{aq}$, shown in figure 9(a),

rapidly decrease as the droplet diameter increases. For example, the density of $H_2O_{2aq}$ decreases more than four orders of magnitude from $2 \times 10^{20}$ cm$^{-3}$ (0.3 M) for a 0.1 $\mu$m droplet to $4 \times 10^{15}$ cm$^{-3}$ ($6 \times 10^{-6}$ M) for a 1 mm droplet. There are three perspectives on this decrease in density. The first is that the same gas production of the precursors of the aqueous species is diluted in a larger volume (i.e. the limit in equation (62)). The second is that for high $h$ and large droplets, the gas phase is depleted of the precursor, thereby decreasing the flux into the surface of the droplet. The third is that the smaller droplets have larger SVRs. The influx of reactive species to the droplet scales with surface area, while density scales with the inverse of volume. Therefore if the incoming fluxes of reactants are constant, in the absence of saturation, smaller droplets will have a larger aqueous density of the solvation partner.

The density of species with the lowest Henry's law constants, $O_{3aq}$, $N_2O_{aq}$, and $H_{2aq}$, shown in figure 9(b), have aqueous densities that are nearly independent of diameter (i.e. the limit in equation (61)). In this case, the aqueous densities are saturated, and do not consume enough of their gas phase precursors to deplete densities in the gas phase. With low Henry's law constants, the liquid densities of these species also tend to remain relatively low, with densities at 5 s being: $O_{3aq}$, $4 \times 10^{15}$ cm$^{-3}$ ($7 \times 10^{-6}$ M); $N_2O_{aq}$, $1 \times 10^{14}$ cm$^{-3}$ ($2 \times 10^{-7}$ M); and $H_{2aq}$. $4 \times 10^{11}$ cm$^{-3}$ ($6 \times 10^{-10}$ M).

Several species deviate from these general trends dictated by low or high Henry's law constants. These deviations are generally due to the consequences of long timescale reactions. $NO_2$ has a Henry's law constant of 0.28. Based on the proposed scaling, $NO_{2aq}$ should fully saturate the droplet and its density should not be directly affected by depletion of gas phase $NO_2$ in this range of diameters. The density of $NO_{2aq}$ does however decrease with increasing droplet diameter. The $NO_{2aq}$ density at the end of the plasma on period is, indeed, nearly independent of diameter. However, there is generation of $NO_{2aq}$ in the afterglow as a result of the decay of $HO_2NO_{2aq}$. $HO_2NO_2$ has a high Henry's law constant and so the density of $HO_2NO_{2aq}$ is sensitive to the depletion of the gas phase densities that occurs at large droplet diameter. This reduction in the density of $HO_2NO_{2aq}$ at large droplet diameters decreases the post-plasma production of $NO_{2aq}$, which decreases its density with increasing droplet diameter. The generation of $NO_{2aq}$ by $HO_2NO_{2aq}$ results in densities as high as $4 \times 10^{13}$ cm$^{-3}$ ($7 \times 10^{-8}$ M) at 5 s which exceeds the Henry's law equilibrium density. As a result, the net flux of $NO_2$ is out of the liquid during the late afterglow.

The density of $HNO_2$ (total of the gas and liquid phase) was larger at smaller droplet diameters. For droplets having diameters 1 $\mu$m or less, $HNO_2$ was at Henry's law equilibrium between the gas phase and droplet, $n_l = hn_g$. For larger droplets, the liquid is not saturated and $n_l \ll hn_g$. The equilibration time for large droplets is longer because of the lower SVR. At the same time, there are losses of $HNO_{2aq}$ in the droplet by reactions with $O_3$ and $N_2O$ at all diameters. These losses scale with the volume of the droplet. For small droplets (large SVR), the rate of solvation of gas phase $HNO_2$ is large enough to replenish the $HNO_{2aq}$ that is lost by volumetric reactions.
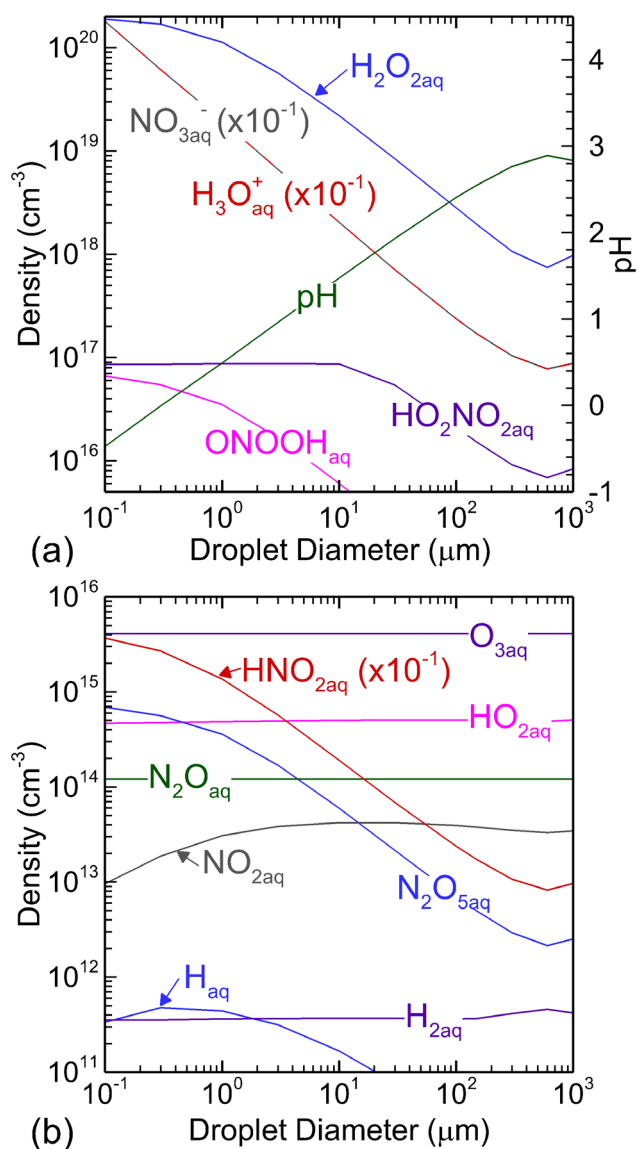


(a)

(b)

**Figure 10.** Density of liquid RONS as a function of droplet diameter in an 'infinite' gas volume ($V_g = 6.3 \times 10^5$) for species with (a) $h \gtrsim 10^5$ and (b) $h \lesssim 10^5$. The data are compared after 500 pulses and an afterglow period for a total time to 5 s. The large gas volume essentially eliminates the effect of depletion of the gas phase RONS.

This enables $HNO_{2aq}$ to remain at equilibrium. For large droplets (small SVR) the rate of replenishment of $HNO_{2aq}$ by solvating $HNO_2$ cannot keep up with the volumetric losses, resulting in a lower $HNO_{2aq}$ density. As a result, the density of $HNO_{2aq}$ decreases from $4 \times 10^{16}$ cm$^{-3}$ ($6 \times 10^{-6}$ M) for a 0.1 $\mu$m droplet to $1 \times 10^{10}$ cm$^{-3}$ ($2 \times 10^{-11}$ M) for a 1 mm droplet.

$H_{aq}$ has a relatively short lifetime in the liquid, as it self-reacts to make $H_{2aq}$ and reacts with $O_{2aq}$ to form $HO_{2aq}$. The conversion of $H_{aq}$ to $HO_{2aq}$ occurs on timescales of ns if $O_{2aq}$ is not depleted. Therefore the significant density of $H_{aq}$ in the afterglow ($5 \times 10^{11}$ cm$^{-3}$, $8 \times 10^{-10}$ M), must be produced by reactions among or decay of more stable RONS. $H_{aq}$ is generated late in the afterglow by the slow decay of $NO_{2aq}^-$ (which is at equilibrium with the corresponding acid $HNO_{2aq}$)

reacting with $H_{3}O_{aq}^{+}$. The dependence of the density of $H_{aq}$ on droplet diameter therefore approximately follows the behavior of $HNO_{2aq}$.

$N_{2}O_{5aq}$ has a Henry's law constant of 48.5 and is under-saturated in the droplet throughout the discharge and afterglow for droplet diameters greater than 1 $\mu$m. $N_{2}O_{5aq}$ reacts with water on timescales of hundreds of $\mu$s to decay into $NO_{2aq}$ and $NO_{3aq}$ or to produce $ONOOH_{aq}$ or $HNO_{3aq}$. Reactions of $NO_{2}$ and $NO_{3}$ in the gas phase produce $N_{2}O_{5}$ at long timescales and solvation of this continuous generation of $N_{2}O_{5}$ helps sustain $N_{2}O_{5aq}$ into the afterglow period. For small enough droplets, this replenishment can compensate for in-droplet losses due to reactions and maintain a near equilibrium. For large droplets, the replenishment is not able to compensate for losses.

$HO_{2}$ has a Henry's law constant of $1.32 \times 10^{5}$. At a droplet diameter of 170 $\mu$m, $hV_{l}/V_{g} = 1$. This diameter marks the transition between droplets in which $HO_{2aq}$ is saturated and so independent of diameter (smaller droplets); and droplets in which the density of $HO_{2aq}$ decreases due to depletion of $HO_{2}$ in the gas phase (larger droplets). For droplets below 10 $\mu$m, the $HO_{2aq}$ density is saturated at $5 \times 10^{14}$ cm$^{-3}$ ($8 \times 10^{-7}$ M). Depletion of gaseous $HO_{2}$ by solvation explains the dependence of the $HO_{2aq}$ on droplet diameters greater than 100 $\mu$m. For 1 mm droplets, the liquid was under-saturated because the equilibration time was on the order of tens of seconds. The increase in the density of $HO_{2aq}$ with diameters between 10 and 100 $\mu$m is due to a decrease in the de-solvation rate. When the diameter is below 170 $\mu$m, the main losses of $HO_{2aq}$ are by de-solvation followed by gas phase reactions with $NO_{2}$. With the de-solvation rate in equation (3), this occurs more slowly as the droplet size increases, resulting in an increase in density as the droplet diameter increases from 10 to 100 $\mu$m.

The primary acid and its conjugate base in this system are $HNO_{3aq}$ and $NO_{3aq}^{-}$. The $H_{3}O_{aq}^{+}$ density is essentially equal to the $NO_{3aq}^{-}$ density for all conditions. With pH being a function of the density $H_{3}O_{aq}^{+}$, it is also for these conditions a function of the production of $NO_{3aq}^{-}$. $HNO_{3}$ has a high Henry's law constant of $4.8 \times 10^{6}$, and its aqueous density is highly sensitive to droplet diameter. The density of $NO_{3aq}^{-}$ and $H_{3}O_{aq}^{+}$ decrease from $1.7 \times 10^{21}$ cm$^{-3}$ (2.8 M) in a 0.1 $\mu$m droplet to $1.6 \times 10^{16}$ cm$^{-3}$ ($2.7 \times 10^{-5}$ M) in a 1 mm droplet. This results in a corresponding increase in pH from $-0.47$ in a 0.1 $\mu$m droplet to 4.56 in a 1 mm droplet.

### 4.3. Droplet diameter: infinite plasma volume

To artificially eliminate the impact of gas phase depletion on activation of the droplet, the base case simulations were repeated with a gas volume of $V_{g} = 6.3 \times 10^{5}$ cm$^{3}$ such that $V_{g} \gg hV_{l}$ for all species at all diameters. The diffusion length was kept the same as in the prior studies discussed in section 2. The resulting aqueous densities, shown in figure 10, do not have a steep decrease for droplets larger than 100 $\mu$m as with the finite gas volume. The depletion of gas phase RONS, rather than SVR, reaction chemistry or equilibration time, was responsible for this steep drop in aqueous densities with a finite gas volume. For example, with a large gas volume, the $H_{2}O_{2aq}$

density in 1 mm droplet is $1 \times 10^{18}$ cm$^{-3}$ ($2 \times 10^{-3}$ M), compared to $4 \times 10^{15}$ cm$^{-3}$ ($6 \times 10^{-6}$ M) when the gas volume is finite.

However, for droplet diameters less than 100 $\mu$m, the aqueous densities of species with high $h$ still depend on diameter. This decrease is a result of the characteristic equilibration time for Henry's law solvation, and the increasing SVR. As the droplet diameter increases, the equilibration time increases as the SVR of the droplet is smaller. With the large volume, the maximum equilibration time occurs with a droplet diameter $\approx 650$ $\mu$m for $h = 10^{0}$–$10^{6}$. With a finite gas volume, the maximum equilibration time occurs for a 30 $\mu$m droplet (figure 8, $h = 10^{6}$). As a result, each of the species which are sensitive to equilibration time ($H_{2}O_{2aq}$, $NO_{3aq}^{-}$, $H_{3}O_{aq}^{+}$, $HO_{2}NO_{2aq}$, $ONOOH_{aq}$, $HNO_{2aq}$, and $N_{2}O_{5aq}$) have an aqueous density that is minimum with a 600 $\mu$m droplet.

The pH is lower (more acidic) for droplets activated in the large gas volume because the densities of $H_{3}O_{aq}^{+}$ and $NO_{3aq}^{-}$ are no longer limited by depletion of the gas phase. The maximum pH of 2.89 occurs for a 600 $\mu$m droplet with the large volume, compared to a maximum of 4.56 when the gas volume was finite. The values of pH of the smaller droplets are unaffected by gas volume. For example, the pH of the 0.1 $\mu$m droplet is $-0.47$, independent of the gas volume, because the densities of $H_{3}O_{aq}^{+}$ and $NO_{3aq}^{-}$ are not limited by depletion.

Although these results demonstrate the importance of gas phase depletion, they do so on a volume averaged basis. In reality, the depletion of gas phase precursors is most severe closest to the droplet. These gradient dependent effects will be discussed with results from the 2D model.

The scaling of most of the densities of low Henry's law species, $O_{3aq}$, $N_{2}O_{aq}$, $H_{2aq}$, and $H_{aq}$ are unchanged by having the large gas volume. The low-$h$ species whose densities significantly changed by increasing the gas volume are $NO_{2aq}$, $N_{2}O_{5aq}$, and $HNO_{2aq}$. The source of $NO_{2aq}$ at long times is primarily the decay of $HO_{2}NO_{2aq}$, which has a high Henry's law constant and is sensitive to gas phase depletion. Eliminating the gas phase depletion of $HO_{2}NO_{2}$ results in an increase in the density of $NO_{2aq}$ in a 1 mm droplet from $3 \times 10^{11}$ cm$^{-3}$ ($6 \times 10^{-10}$ M) to $3 \times 10^{13}$ cm$^{-3}$ ($6 \times 10^{-8}$ M). Even though $HO_{2aq}$ has a large $h$ ($1.32 \times 10^{5}$), its density remains nearly constant with droplet diameter, because it no longer depletes the gas phase for diameters above 170 $\mu$m.

$N_{2}O_{5aq}$ has a Henry's law constant of 48.5 and is produced primarily from solvation of gaseous $N_{2}O_{5}$. The lifetime of $N_{2}O_{5aq}$ is hundreds of $\mu$s. With this short lifetime, $N_{2}O_{5aq}$ must be replenished by solvation from the gas phase to maintain its density. As a result, the long-time density of $N_{2}O_{5aq}$ depends on the SVR of the droplet, which decreases with increasing droplet diameter. Smaller SVR is unable to replenish $N_{2}O_{5aq}$ rapidly enough to offset losses due to volumetric reactions. The dependence of $N_{2}O_{5aq}$ on droplet diameter and gas phase depletion also results from cyclic synergistic processes between the droplet and gas phase reactants. These processes involve $HO_{2}NO_{2aq}$, a precursor for $N_{2}O_{5aq}$ production at long times. The decay of $HO_{2}NO_{2aq}$ produces $NO_{2aq}$ which
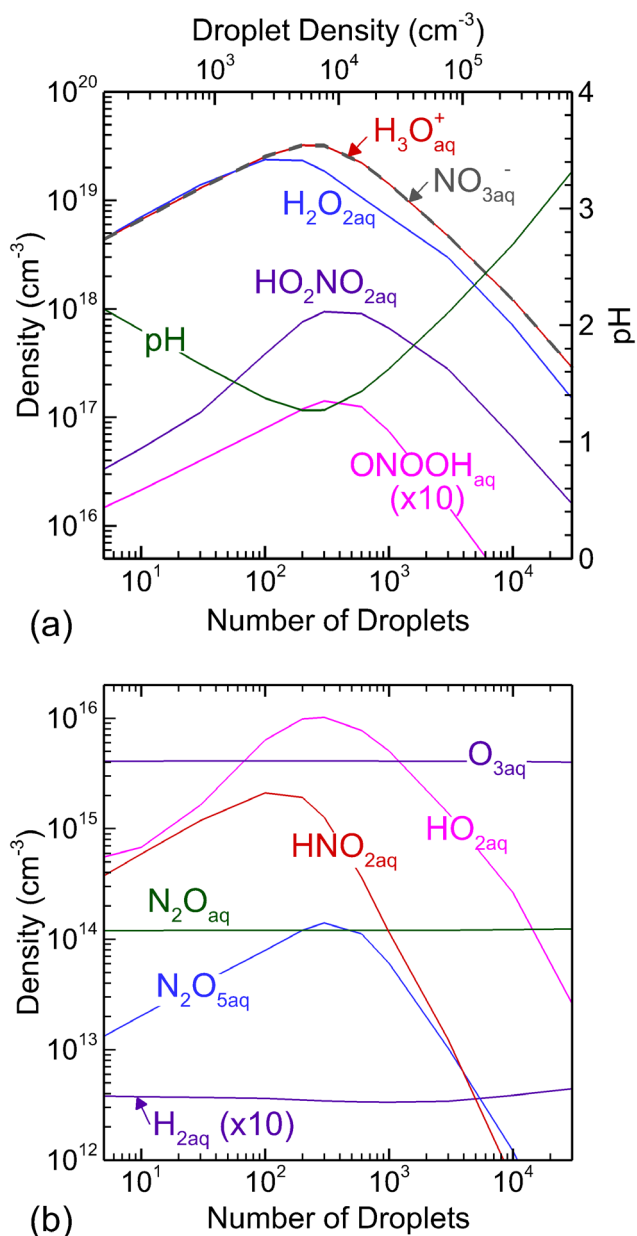
**Figure 11.** Density of liquid RONS as a function of the number of 10 $\mu$m droplets for species with (a) $h \gtrsim 10^5$ and (b) $h \lesssim 10^5$. The densities were compared after 5 s total time.
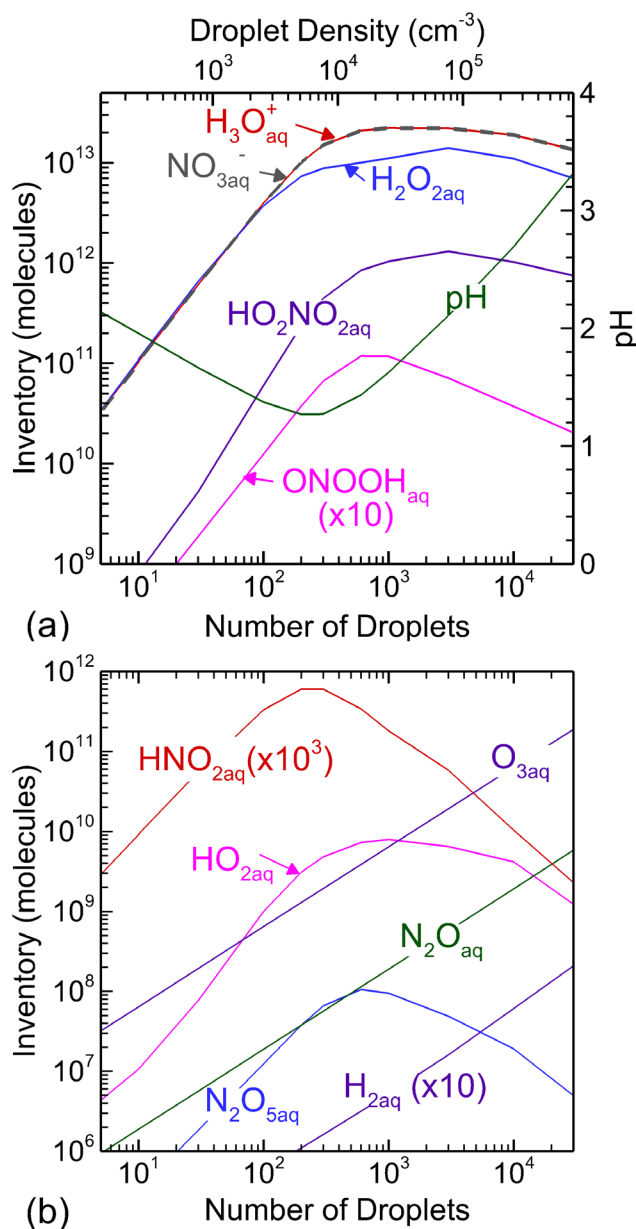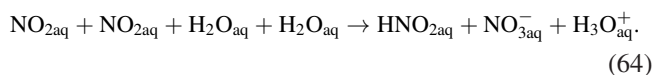


**Figure 12.** Inventory of liquid RONS with (a) $h \gtrsim 10^5$ and (b) $h \lesssim 10^5$ as a function of the number of droplets having a 10 $\mu$m diameter. The inventory is the aqueous number density multiplied by the total liquid volume. The inventories are compared after 5 s total time.

becomes oversaturated and de-solvates into gaseous NO$_2$. The NO$_2$ then reacts with O$_3$ to produce NO$_3$, which reacts with an additional NO$_2$ to form N$_2$O$_5$. This N$_2$O$_5$ then solvates, forming N$_2$O$_{5aq}$ long into the afterglow.

HNO$_2$ has a Henry's law constant of $1.15 \times 10^3$. The density of HNO$_{2aq}$ for a 1 mm droplet in a large gas volume is $1 \times 10^{14}$ cm$^{-3}$ ($2 \times 10^{-7}$ M) compared to $1 \times 10^{10}$ cm$^{-3}$ ($2 \times 10^{-11}$ M) for the small volume. HNO$_{2aq}$ reacts with O$_{3aq}$ and N$_2$O$_{aq}$ which have densities nearly independent of droplet diameter. The replenishment of HNO$_{2aq}$ is by solvation of HNO$_2$. However this replenishment decreases with increasing droplet diameter due to the decreasing SVR. HNO$_{2aq}$ is sensitive to gas phase depletion because the steady state density of HNO$_{2aq}$ in the afterglow is a result of a reaction involving NO$_{2aq}$,

$$NO_{2aq} + NO_{2aq} + H_2O_{aq} + H_2O_{aq} \rightarrow HNO_{2aq} + NO_{3aq}^- + H_3O_{aq}^+. \tag{64}$$

As a result, the HNO$_{2aq}$ density at large droplet diameter increases when gas phase depletion is not a factor due to the now larger NO$_{2aq}$ densities.

### 4.4. Number of droplets

To extend this study to a technologically more relevant parameter space, the number of droplets in the system was increased to simulate an aerosol. To increase the droplet density, the liquid volume and surface area were increased, the gas volume was decreased, and the diffusion length was defined as the

J. Phys. D: Appl. Phys. **52** (2019) 355207

J Kruszelnicki *et al*

average distance between the droplets divided by $\pi$. The droplet diameter was fixed at 10 $\mu$m. The droplet density, or the number of droplets per reactor volume, had a significant impact on the liquid activation, as shown in figures 11 and 12. The maximum activation for this system occurred with 300 droplets, or $7.6 \times 10^3$ droplets cm$^{-3}$.

The densities of the stable low-*h* species, $O_{3aq}$, $N_2O_{aq}$, and $H_{2aq}$, were independent of the number of droplets, limited by the Henry's law saturation of the liquid (densities are shown in figure 11). These species also equilibrate quickly because of their low Henry's law constant, and were therefore relatively independent of diffusion length which would increase (or decrease) fluxes to the surface of the droplet.

The densities of species with higher *h*, on the other hand, were sensitive to the number of droplets. If the number of droplets was too low, the solvation was transport limited by the large diffusion length. The equilibration times were on the order of tens of seconds for 3 droplets in the gas volume. The diffusion length was large, and on average the plasma produced species had further to diffuse before reaching the droplet surface. However, if there are too many droplets, the activation becomes limited by depletion of the gas phase RONS, effectively diluting the RONS in a larger liquid volume.

For example, $HO_2NO_{2aq}$ has a density of $2 \times 10^{16}$ cm$^{-3}$ ($4 \times 10^{-5}$ M) for three droplets in the gas which increases to $8 \times 10^{17}$ cm$^{-3}$ ($1 \times 10^{-3}$ M) for 200 droplets. When the number of droplets is further increased and the $HO_2NO_{2aq}$ is diluted into a larger total volume of liquid, the density decreases to $2 \times 10^{16}$ cm$^{-3}$ ($3 \times 10^{-5}$ M) for 30 000 droplets. Since $NO_{3aq}^-$ is sensitive to both equilibration time and depletion of gaseous $HNO_3$, its density also has a maximum at 300 droplets. As a result, pH (a function of $H_3O_{aq}^+$ and $NO_{3aq}^-$ in this system) has a minimum of 1.3 for 300 droplets. In contrast for 30 000 droplets, $H_3O_{aq}^+$ and $NO_{3aq}^-$ are diluted and the pH is 3.3.

The inventory of aqueous species is the average density in individual droplets multiplied by the total liquid volume. The total inventory of reactive species is the metric of interest when, for example, using an activated aerosol spray to treat a surface. These inventories of RONS are shown in figure 12 as a function of number of droplets. Stable species with low *h* ($O_{3aq}$, $N_2O_{aq}$, and $H_{2aq}$) have inventories that are nearly linear functions of the number of droplets because their densities in individual droplets do not vary. For example, the inventory of $O_{3aq}$, increases from $2 \times 10^7$ to $2 \times 10^{11}$ when increasing the number of droplets from 3 to 30 000. $H_2O_{2aq}$, $NO_{3aq}^-$, $H_3O_{aq}^+$, and $HO_2NO_{2aq}$, have inventories that are nearly constant above $10^3$ droplets in the volume. The maximum inventories of $NO_{3aq}^-$ and $H_3O_{aq}^+$ are both $2 \times 10^{13}$ molecules, while inventories of $H_2O_{2aq}$ are maximum at $1 \times 10^{13}$ and of $HO_2NO_{2aq}$ at $1 \times 10^{12}$. The nearly constant inventories above $10^3$ droplets indicates that the decrease in the density of these species with increasing number of droplets (figure 11) was due to diluting the same number of molecules into a larger volume of liquid.

$ONOOH_{aq}$, $HNO_{2aq}$, $HO_{2aq}$, and $N_2O_{5aq}$ experience significant decreases in inventory above $10^3$ droplets. For example,
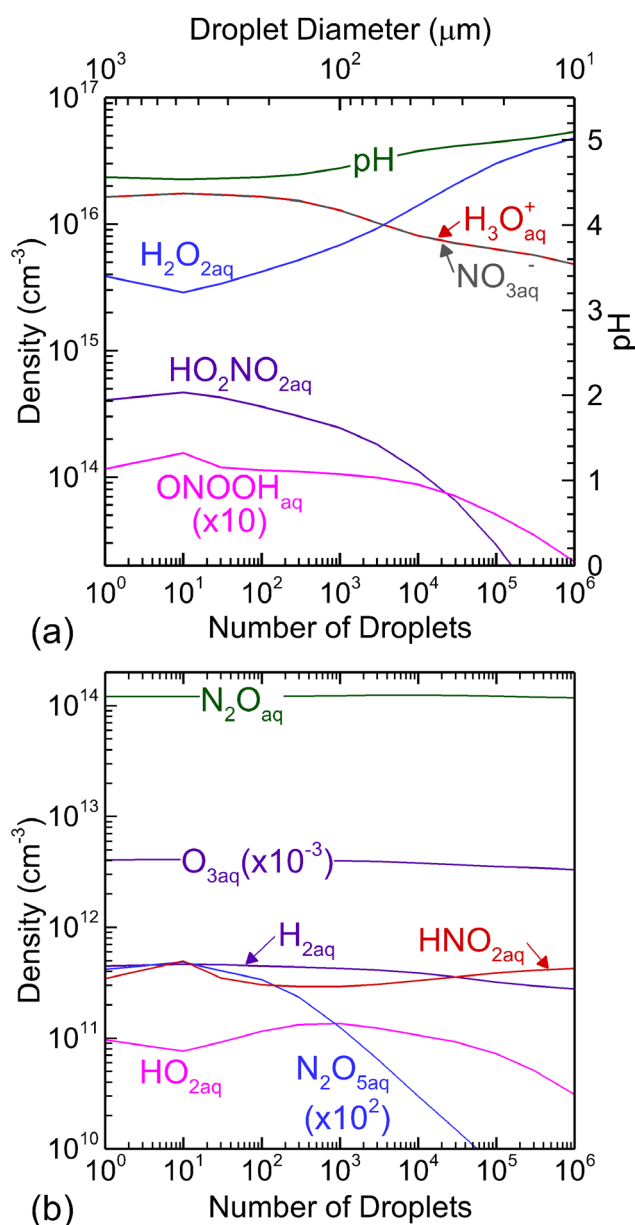


**Figure 13.** Liquid species densities as a function of the number of droplets. The total liquid volume was held constant and the diameter was decreased as the number of droplets was increased. The densities were compared at 5 s total time for species with (a) $h \gtrsim 10^5$ and (b) $h \lesssim 10^5$.

the inventory of $ONOOH_{aq}$ is maximum at $1 \times 10^{11}$ molecules for 600 droplets, and decreases to $2 \times 10^{10}$ molecules for 30 000 droplets. These species are slightly less stable as they undergo long timescale reactions after solvating. The decrease in their inventories can be attributed to shorter equilibration times and smaller diffusion lengths resulting in more rapid solvation. These species all decay in the liquid, so increasing the solvation rate (smaller $\Lambda$) results in the aqueous densities rising more rapidly in the afterglow (shorter equilibration time). They then become depleted in the gas phase more quickly, resulting in a lower flux of these species into the droplet later in the afterglow. The lower incoming fluxes are then unable to replenish losses by reactions as they convert to

J. Phys. D: Appl. Phys. **52** (2019) 355207

J Kruszelnicki *et al*

$NO_{3aq}^-$. For example, for 600 droplets, the $HNO_{2aq}$ inventory slowly decreases from $2 \times 10^{10}$ at the end of the pulsing period to $9 \times 10^8$ by 5 s as it is replenished by solvation from the gas phase. For $3 \times 10^4$ droplets, the inventory of $HNO_{2aq}$ rapidly decreases from $3 \times 10^{11}$ at the end of the pulsing period to $6 \times 10^6$ by 5 s. So for the densities shown in figure 11, the decrease above $10^3$ droplets was in part due to the dilution, but also due to the more rapid solvation and conversion of species to their final products.

### 4.5. Dispersing a finite volume of water into droplets

In optimizing, for example, a plasma activated water spray of droplets having a given flow rate (or volume) of liquid, a decision must be made about the number and diameter of the droplets. This optimization was investigated using the volume of liquid for a 1 mm droplet and dispersing that constant volume into a different number of droplets having the appropriate diameters to maintain constant volume. In the global model, this was accomplished by adjusting the diffusion length and area of plasma contacting the liquid. The results of this study are shown in figure 13.

In this parameterization, $V_g/V_l$ remains constant while the diffusion length varies. Species with higher Henry's law constants are more sensitive to diffusion length because they have longer equilibration times. $O_{3aq}$, $N_{2aq}$, and $H_{2aq}$ were less affected by the method of dispersal of the droplets because they rapidly saturate the liquid, even for a single 1 mm droplet, due to their low Henry's law constants.

The high-$h$ species were more sensitive to the method of dispersal. Most of the densities of RNS decreased with increasing number of droplets while the density of $H_2O_{2aq}$ increased. The $H_2O_{2aq}$ density was minimum at $3 \times 10^{15}$ cm$^{-3}$ ($8 \times 10^{-5}$ M) for 10 droplets and increased to $5 \times 10^{16}$ cm$^{-3}$ ($6 \times 10^{-5}$ M) for $10^6$ droplets. The densities of $NO_{3aq}^-$ and $H_3O_{aq}^+$ showed the opposite trend, with maxima of $2 \times 10^{16}$ cm$^{-3}$ ($3 \times 10^{-5}$ M) for 10 droplets and $5 \times 10^{15}$ cm$^{-3}$ ($8 \times 10^{-6}$ M) for $10^6$ droplets.

A larger number of smaller droplets resulted in a larger SVR and a shorter diffusion length. These factors both increased the fluence of reactive species that have short gas phase lifetimes that reached the droplets, such as ions, electronically excited states, and O. When striking the water surface, these species were much more likely to dissociate $H_2O_{aq}$, rather than react with $N_2$ or $O_2$ in the gas phase. For example, the pathway for electronically excited states is

$$M^* + H_2O_{aq} \rightarrow M_{aq} + H_{aq} + OH_{aq}, \tag{65}$$

$$OH_{aq} + OH_{aq} \rightarrow H_2O_{2aq}. \tag{66}$$
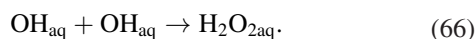
OH that was formed in the gas phase was more likely to solvate when the diffusion length was smaller, rather than reacting with $N_xO_y$ to form $HNO_x$. As a result, the pulsed periodic equilibrium density of $OH_{aq}$ increases by more than a factor of four across the range of droplets investigated. Therefore dividing a liquid volume into many smaller droplets resulted in more $H_2O_{2aq}$ than $NO_{3aq}^-$.
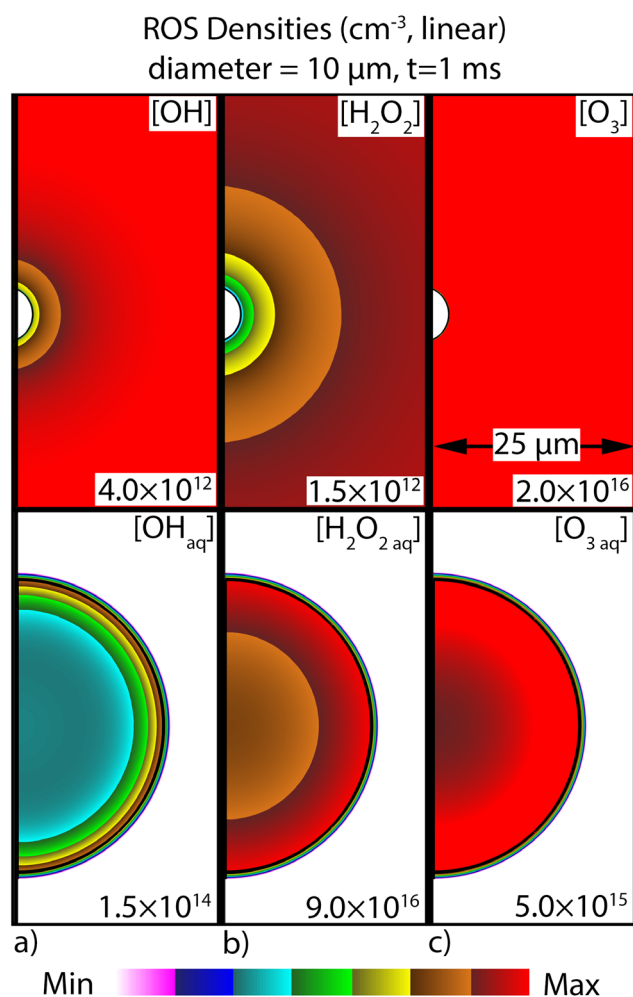


**Figure 14.** Local densities of gas-phase (top) and solvated (bottom) species after 1 ms in the reactive diffusion base case (droplet diameter = 10 $\mu$m). Maximum values are noted in each frame. (a) OH, (b) $H_2O_2$, (c) $O_3$. $OH_{aq}$ is confined to the near surface of the droplet. Local depletion of gas phase $H_2O_2$ near the droplet is due to its high $h$ enabling continuous solvation while there is little gas phase depletion of $O_3$.

## 5. Consequences of in droplet transport and plasma spatial gradients

While global modeling enables significant insights into long-term chemistry, the inherent assumption of a well-mixed reactor does not account for spatial gradients beyond those that can be accommodated by a diffusion length. To resolve spatial gradients in densities, the plasma-droplet system was modeled using the 2D plasma hydrodynamics model, *nonPDPSIM*. Two studies were performed with an increasing degree of spatial variation. First, a single droplet was inserted into a gas region in which densities of reactive species were initially uniform (see figure 2(a)). The initial densities of gas phase species were obtained from a *GlobalKin* simulation after 500 pulses at 10 kHz, and are listed in table 2. The water droplet was initialized as a liquid $H_2O$ with equilibrium densities of solvated $O_2$ and $N_2$ and a pH of 7. This computational approach addresses depletion of gas-phase species near the droplet as they solvate into the

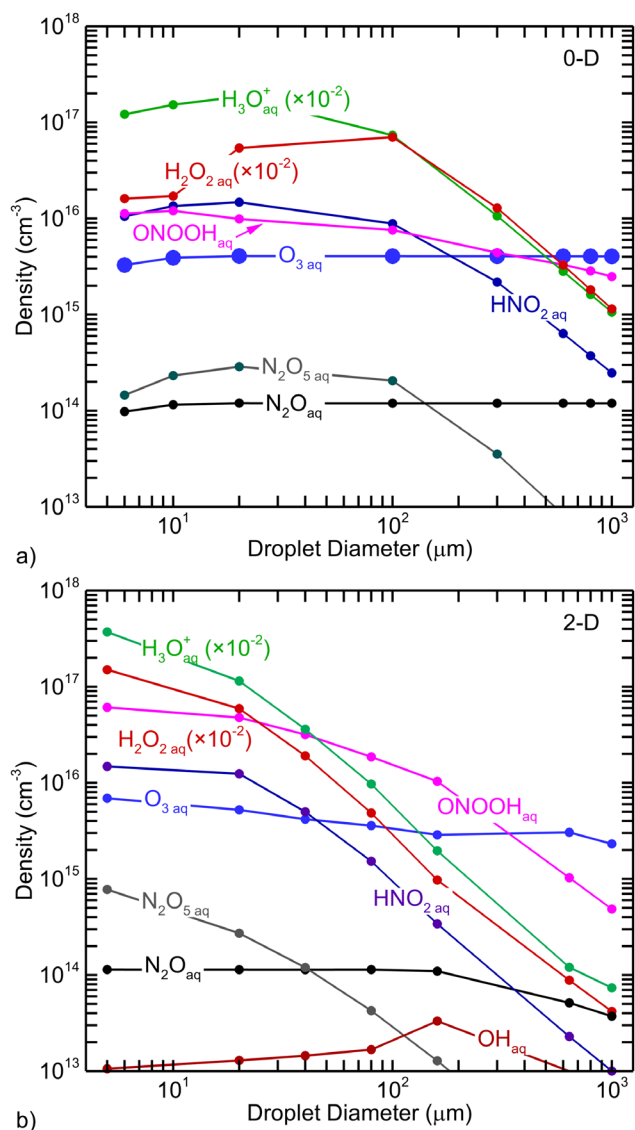J. Phys. D: Appl. Phys. **52** (2019) 355207

J Kruszelnicki *et al*



**Figure 15.** Average densities of liquid-phase RONS as a function of droplet diameter after 200 ms using (a) the global model and (b) the 2D model after 200 ms. The densities of stable, high-*h* species strongly depend on droplet diameter. Stable, low-*h* species have average densities considerably less sensitive to droplet diameter.

turned off. This approach is conceptually similar to global modeling while accounting for local gradients both in the gas phase and in the droplet. The base case has a 10 $\mu$m droplet at the center of a cylindrically symmetrical reactor with a height of 0.46 mm and radius of 0.23 mm. The densities of liquid and gas-phase OH, $H_2O_2$, and $O_3$, are shown in figure 14 after 1.0 ms. The mean lifetime of $OH_{aq}$ in the liquid is approximately 200 $\mu$s, which is reflected in its short penetration distance into the droplet, as shown in figure 14(a). The $OH_{aq}$ densities are highest at the surface of the droplet, with $OH_{aq}$ combining to form $H_2O_{2aq}$ before diffusing into the interior of the droplet. However, the main source of $H_2O_{2aq}$ is not hydroxyl reactions in the droplet but rather solvation of $H_2O_2$ from the gas-phase. A depletion region of $H_2O_2$ forms near the surface of the droplet as $H_2O_2$ rapidly solvates (figure 14(b)). The Henry's law constant for $H_2O_2$ is high ($h = 1.92 \times 10^6$), so the droplet can support liquid-phase densities which are six orders of magnitude greater than those in the gas-phase before saturating. The opposite is true for ozone ($h = 0.274$). The droplet quickly saturates with $O_{3aq}$ and solvation from the gas phase ceases. No local gas phase depletion occurs (figure 14(c)).

The average aqueous densities of selected species obtained with the 2D model after 200 ms as a function of droplet diameter are shown in figure 15. These results mirror those from the global simulations, also shown in figure 15. The aqueous densities of high-*h*, stable species are sensitive to droplet diameter. The densities of $H_2O_{2aq}$ decreased from $1.5 \times 10^{16}$ cm$^{-3}$ ($2.5 \times 10^{-5}$ M) for a droplet diameter of $d = 10$ $\mu$m to $1.0 \times 10^{14}$ cm$^{-3}$ ($2.0 \times 10^{-6}$ M) for $d = 2$ mm. Similarly, the average density of hydronium $H_3O_{aq}^+$ decreased from $2.0 \times 10^{18}$ cm$^{-3}$ ($3.3 \times 10^{-3}$ M) to $1.0 \times 10^{16}$ cm$^{-3}$ ($1.7 \times 10^{-5}$ M) resulting in an increase in average pH (2.5 at $d = 10$ $\mu$m, to 4.8 at $d = 2$ mm). Low-*h* and long lived aqueous species had densities that were nearly independent of droplet diameter. The change in $O_{3aq}$ density, for example, was less than 10% when increasing the droplet diameter from 5 $\mu$m and to 1 mm. As discussed for the global modeling, when high-*h* gas phase species solvate and fail to saturate the droplet, their local gas densities are depleted around the droplet, leading to lower rates of solvation in the afterglow. The effect is more dramatic when accounting for local depletion and gradients around the droplet, which then increases the effective distance from the droplet from which the solvating species originate.

A comparison of the aqueous chemistry obtained with the global and 2D models after 200 ms is shown in figure 15. These modeling approaches represent two limits of gas–liquid transport. With the options used in the 2D model, the results represent the diffusive limit on reactant transport, where convection is negligible, the surface of the liquid can saturate, and local depletion occurs in the gas phase. The global model, represents infinitely rapid convection in the liquid and gas phase by using a well-stirred reactor approximation in both phases. The actual experimental behavior will lie between these extremes depending on experimental conditions. In general, the qualitative trends shown in figure 15 between the two models are in agreement. The aqueous densities of stable,

droplet. The second study increased spatial complexity by placing a droplet at a center of a DBD (see figure 3) having a single plasma filament. Full plasma calculations were then performed resulting in the development of a microdischarge channel. The densities of gas-phase reactive species therefore varied as a function of distance from the droplet. The intent of this simulation was to demonstrate a worst case of how the non-uniformity of the plasma can affect solvation of reactants into a droplet and de-solvation of reactants out of a droplet.

### 5.1. Reaction-diffusion: uniform initial gas-phase densities

Simulating a droplet interacting with uniformly distributed gas-phase species emulates a diffuse plasma reactor or a droplet entering a reactor directly after the plasma has been

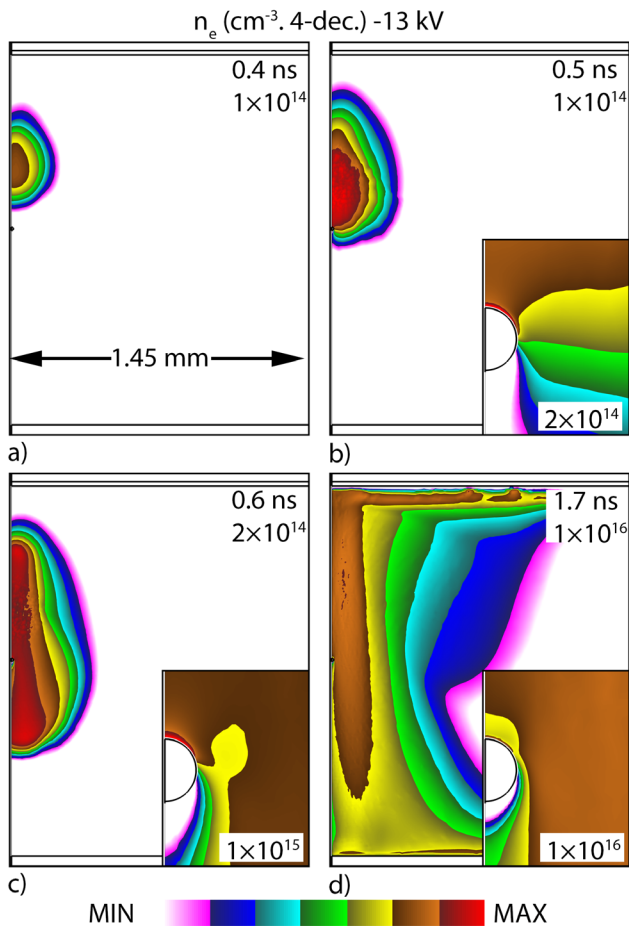J. Phys. D: Appl. Phys. **52** (2019) 355207

J Kruszelnicki *et al*



**Figure 16.** Evolution of electron density in the DBD for the base-case (10 $\mu$m droplet). Images are at (a) 0.4 ns, (b) 0.5 ns, (c) 0.6 ns and (d) 1.7 ns. The embedded figures are close-ups of the volume near the droplet. An upwards restrike from the top of the droplet occurs while the downward moving microdischarge envelops the droplet. Anisotropies in distribution of electron densities develop. Images are plotted on a 4-decade log scale with peak values noted in the figures.



**Figure 17.** Evolution of the electron impact ionization source in the DBD for the base-case (10 $\mu$m droplet). Images are at (a) 0.4 ns, (b) 0.5 ns, (c) 0.6 ns and (d) 1.7 ns. The embedded figures are close-ups of the region near the droplets. Images are plotted on a 2-decade log scale with peak values noted in the figures.

low-$h$ species (e.g. $N_2O_{aq}$, $O_{3aq}$) have little dependence on the diameter of the droplet. The densities of $HNO_{xaq}$, $H_3O_{aq}^+$, and $H_2O_{2aq}$ conversely have strong dependence on diameter of the droplet, with their average densities decreasing as the surface to volume ratio (SVR) decreases.

Quantitatively, the densities are also similar, with most being within 1 order of magnitude between the two models. The decrease in the densities of high-$h$ species predicted for small droplet diameter in the global model, is not observed in the 2D results. This decrease is due to differences in initial conditions. In the global model, the droplets were present during the pulsing of the plasma. This allowed additional recombination and quenching pathways, particularly in droplets with diameters below 20 $\mu$m.

### 5.2. Droplet activated by a single filament DBD

The geometry in figure 3 was used to simulate a single filament DBD sustained in humid air interacting with a single droplet, enabling analysis of the discharge dynamics as well
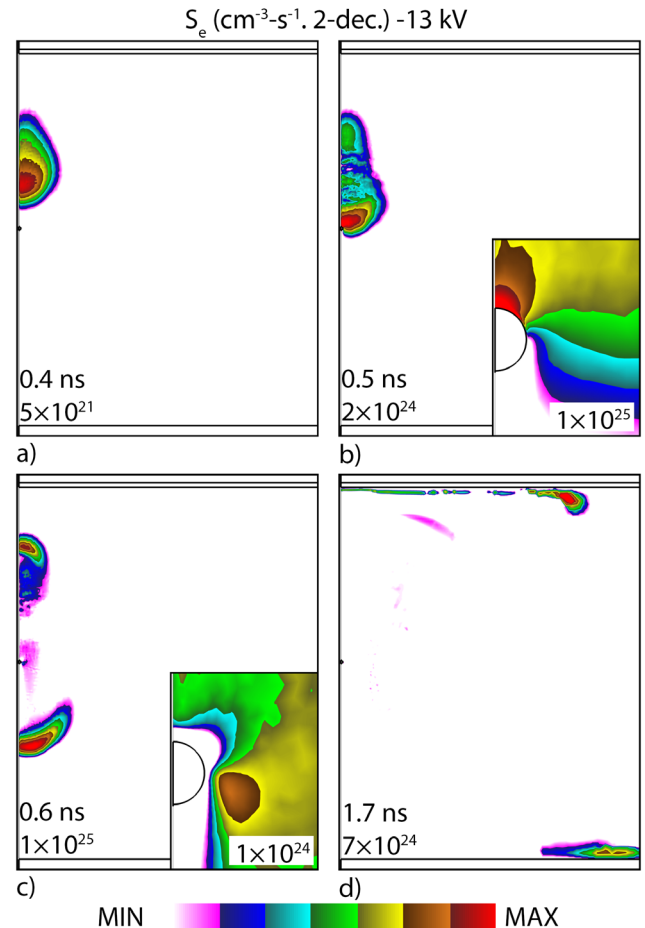
as the effect of non-isotropic distributions of reactive species. The single filament represents a worst-case for how non-uniform discharges may affect rates of solvation and desolvation. A high repetition rate DBD would normally have, on the average, a more uniform distribution of filaments and reactants.

A step pulse of $-13$ kV was applied to the cathode and held constant for approximately 2 ns—sufficient for the development of a microdischarge in this 1 mm gap. The applied electric field is $\approx$500 Td or 120 kV cm$^{-1}$. Assuming typical values for conductivity and permittivity of ultra-pure water ($5.5 \times 10^{-8}$ S cm$^{-1}$ and $7.1 \times 10^{-12}$ F cm$^{-1}$), the dielectric relaxation time of the droplet is approximately 0.13 ms [66, 67]. As a result, the liquid behaves like a dielectric over the time-scale of the discharge. When the external electric field is applied, dielectric polarization of the droplet leads to regions of electric field enhancement at the vertical poles of the droplet, with a peak of $\approx$1200 Td or 310 kV cm$^{-1}$, as shown in figure 3(d). This electric field enhancement increases the likelihood of discharge formation in the vicinity of the droplet.

The electron density ($n_e$) and electron impact ionization source ($S_e$) are shown as a function time in figures 16 and

## Density (cm⁻³, 4 dec.),
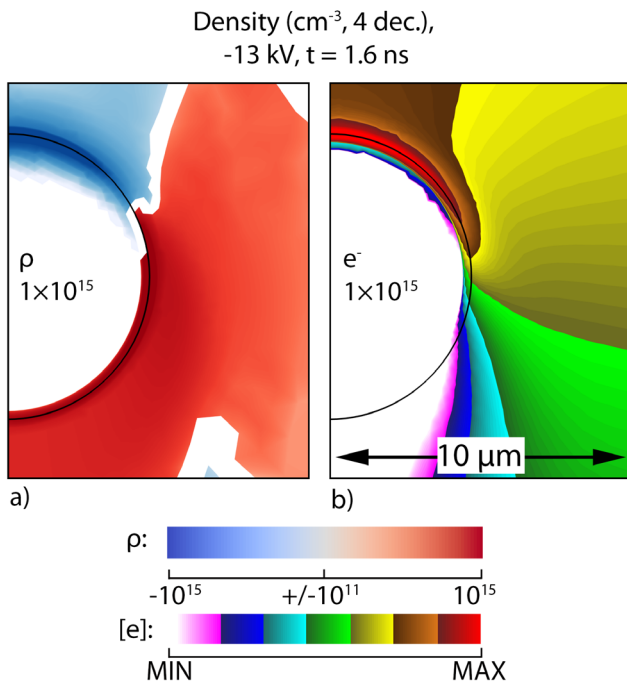## -13 kV, t = 1.6 ns



**Figure 18.** Electrical properties of the droplet. (a) Charge density (sum of densities of all charged species) and (b) sum of solvated and gas-phase electrons around and in the 10 $\mu$m droplet at the end of a single pulse. (a) Blue indicates net negative density and red shows net positive density. The top vertical pole of the droplet becomes negatively charged as electrons in the negative downward directed discharge solvate. Other regions of the droplet become positively charged.

17. Following application of the negative voltage, charge separation occurs in the initial plasma cloud, with electrons accelerating downward towards ground. This initial phase resembles a Townsend avalanche, with a local peak electron density $\approx 3 \times 10^{13}$ cm⁻³ and peak electron-impact ionization rate of $5.5 \times 10^{23}$ cm⁻³ s⁻¹ (figures 16(a) and 17(a)). Upon approaching the droplet, the avalanche enters the region of electric field enhancement produced by the dielectric polarization. The high electric field produces an increase in $T_e$ (maximum $\approx 10.6$ eV) and in $S_e$ (maximum $\approx 4.5 \times 10^{24}$ cm⁻³ s⁻¹) near the droplet surface (figure 17(b)). The electron density then increases to $\approx 1.5 \times 10^{14}$ cm⁻³ in the same region (figure 16(b)).

Following this initial interaction between the plasma and droplet, a cathode-seeking restrike propagates upwards from the surface of the droplet. Simultaneously, the primary (negative) IW propagates downwards around the droplet towards ground. The region directly beneath the droplet is temporarily shielded from the plasma by charging of the surface, leading to anisotropy in the charge distribution (figure 16(c)). By $t = 1.15$ ns, a microdischarge bridges the entire gas gap, and envelops the droplet in plasma. Simultaneously, SIWs develop along the dielectric covering both electrodes, with the electron density reaching its maximum value of $8.5 \times 10^{15}$ cm⁻³ near the cathode. The electron density near the droplet is maximum at $1.95 \times 10^{14}$ cm⁻³ at its top vertical pole. In spite of the locally high electric field, the region near the bottom pole of the droplet does not undergo breakdown due to the droplet

shielding the initial negative streamer. This then leads to a change in polarity of surface charging between the top and bottom poles of the droplet. The combination of the restrike produced by polarization of the droplet and shielding of the initial avalanche by the droplet itself produces an initially anisotropic distribution of ions, excited states and radicals around the droplet.

With the conductivity of the droplet initially being low, the charges solvating into the outer layers of the droplet do not dissipate on short time-scales, leading to what appears to be surface charging analogous to a solid. Charging of the droplets can lead to electrostatic interactions. For example, Grashchenkov and Grigoryev found that closely spaced charged evaporating droplets can coalesce due to attractive polarization forces. When like-charged droplets have larger separations, Coulomb repulsion was found to dominate [68]. Maguire *et al* investigated radio frequency plasma-water droplet interactions. They found that the plasma affects the movement and evaporation rates of the droplets, indicating charging and surface chemistry effects [69]. However, such electro-hydrodynamic effects producing droplet motion are outside of the scope of this study.

With the exception of the top vertical pole (where the initial negative discharge first intersects with the droplet), the outer layer of the droplet is initially positively charged. The net charge density and the density of gaseous and solvated electrons are shown in figure 18 at $t = 1.6$ ns. The maximum charge density in the positive region was 1.9 $\mu$C cm⁻³, primarily due to solvation of gas-phase cations to form $H_2O_{aq}^+$ ($1.9 \times 10^{12}$ cm⁻³), $O_{2aq}^+$ ($1.4 \times 10^{12}$ cm⁻³), and $N_{4aq}^+$ ($1.3 \times 10^{12}$ cm⁻³). (On these short time scales, charge exchange to the water and formation of hydronium have not yet occurred.) The liquid-phase densities closely follow the distribution of their gas-phase precursors. In the negatively-charged region, the peak charge density was approximately two orders of magnitude greater, $-240$ $\mu$C cm⁻³, due primarily to solvating electrons. Once solvated, the low mobilities of charged species in the droplet impedes their drift and diffusion into the interior of the droplet, giving the appearance of surface charging.

As electrons enter the liquid, they quickly solvate and their mobility further decreases. The nature of electron solvation from plasmas is an active area of research [70]. In our model, an electron entering into the droplet reacts with a water molecule to form what appears to be a water negative ion, $H_2O\text{-}e_{aq}^-$. The rate coefficient for this reaction was set based on work of Rumbach *et al* [71] who estimated the penetration depth of solvated electrons into water to be between 2.5 nm and 12.5 nm. We set the rate coefficient for the solvation reaction so that the electrons would solvate at the first node of the liquid surface during full plasma calculation. As a result, there is a large accumulation of solvated electrons at the upper pole of the droplet having a peak density ($1.3 \times 10^{15}$ cm⁻³) at $t = 1.8$ ns. The solvated electrons then charge exchange to liquid-phase anions, including $O_{aq}^-$ ($\approx 2.1 \times 10^{11}$ cm⁻³, $3.5 \times 10^{-8}$ M), $OH_{aq}^-$ ($\approx 3.5 \times 10^{10}$ cm⁻³, $5.8 \times 10^{-11}$ M), and $O_{2aq}^-$ ($\approx 1.5 \times 10^{10}$ cm⁻³, $2.5 \times 10^{-11}$ M), the latter due to attachment to dissolved $O_2$. With time, gas-phase positive
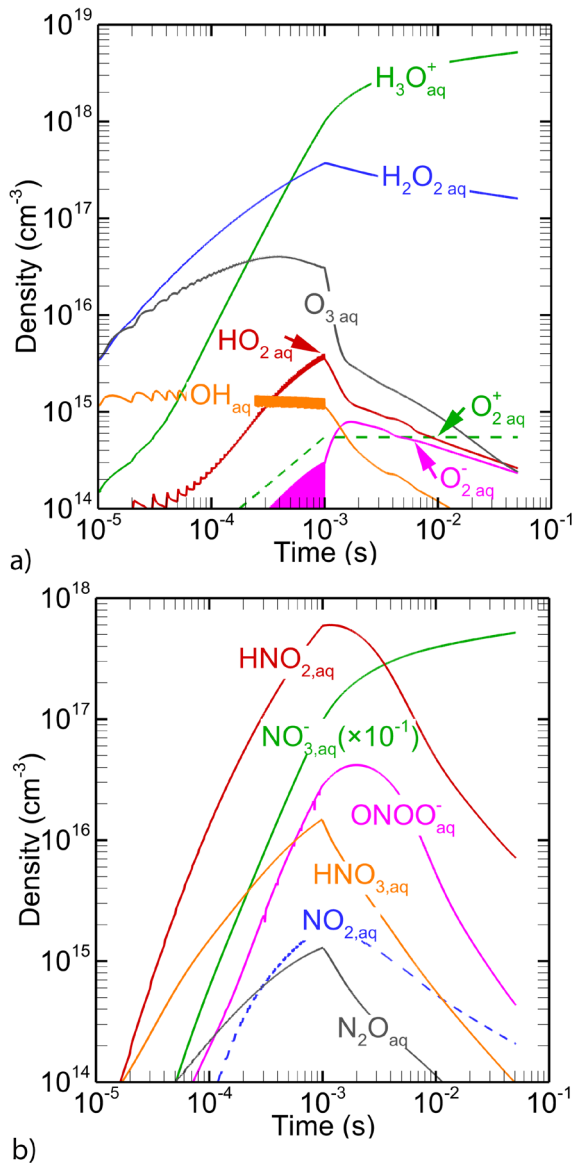
a)

**Figure 19.** Time evolution of the average aqueous densities of (a) ROS and (b) RNS in the base case over 100 pulses lasting to 1 ms followed by afterglow to 50 ms. Note the density of $O_{3aq}$ peaking at $t = 1$ ms, then sharply decreasing due to de-solvation following the cessation of pulsing.

ions drift into to the negative regions of the droplet, thereby reducing the net charge.

The maximum amount of charge that can be stored by a liquid droplet can be estimated using the Rayleigh Limit [72]:

$$q^2 = 64\pi^2\varepsilon_0\gamma a^3, \tag{67}$$

where $q$ is the stored charge, $\varepsilon_0$ is the permittivity of free space, $\gamma$ is the surface tension of the droplet, and $a$ is its radius. As the electrostatic force overcomes the surface tension of the liquid, a droplet becomes unstable. Using the surface tension of a pure water droplet with radius of 5 $\mu$m in air at 1 atm, the charge limit is approximately 0.25 pC or $1.6 \times 10^6$ elementary charges. In these simulations, the charge in the droplet at the end of the discharge pulse was below the Rayleigh limit, with an average charge density $-72.1$ $\mu$C cm$^{-3}$, which when volume-integrated yield a total charge of $-37.8$ fC.
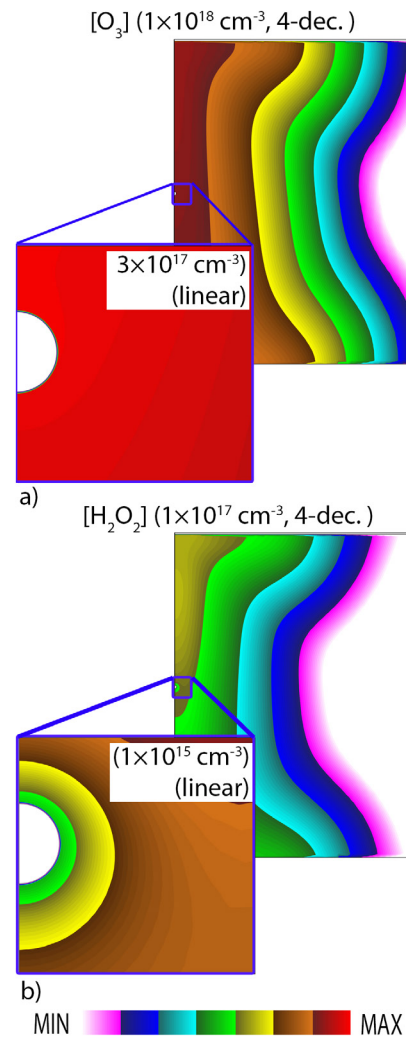


**Figure 20.** Densities of (a) gas-phase $O_3$ and (b) $H_2O_2$ near the droplet at the end of pulsing at 1 ms. A depletion region around the droplet occurs for high-*h* species.

On the timescale of the discharge pulse, the primary anions produced in the droplet are $O_{2aq}^-$, $O_{aq}^-$, and $OH_{aq}^-$. Cations solvate and produce $H_2O_{aq}^+$ on nanosecond time-scales. On longer timescales, terminal liquid-phase ions are $H_3O_{aq}^+$ and $NO_{3aq}^-$. They are primarily produced by hydrolysis of solvated acids. The lowest pH ($\approx 6.90$) at the end of the first pulse is near the top of the droplet where the initial IW interacts with the liquid.

### 5.3. Inter-pulse chemistry and local depletion

The discharge pulse described in the previous section was repeated at a frequency of 100 kHz—corresponding to a 10 $\mu$s inter-pulse period—for 100 pulses having an elapsed time of 1 ms, followed by a 49 ms afterglow for a total time of 50 ms. This burst of high repetition rate pulses was deliberately chosen so that large densities of discharge products would be produced in a small volume after which diffusion would significantly reduce their local densities. The goal is to demonstrate how spatial gradients in gas phase precursors can affect liquid phase chemistry.
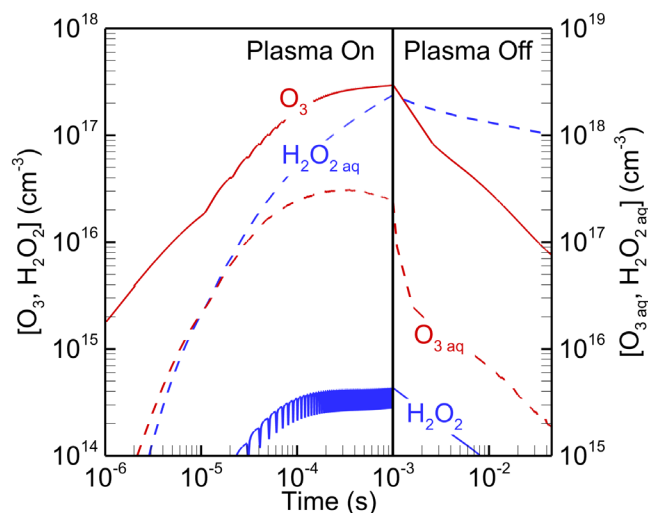
**Figure 21.** Time evolution of the densities of liquid- and gas-phase $O_3$ and $H_2O_2$ directly inside and outside of the droplet. The $H_2O_{2aq}$ density remains relatively stable as it has not yet saturated the droplet whereas the density of $O_{3aq}$ decreases as it de-solvates to maintain equilibrium.

The aqueous densities of ROS and RNS in the droplet are shown in figure 19 as a function of time. At the end of pulsing the discharge ($t = 1$ ms) the systematic behavior of aqueous densities is largely determined by Henry's Law constants. As with the global modeling, the trends of densities of hydrogen peroxide and ozone will be compared as both species are relatively stable and have similar diffusion coefficients while having vastly different Henry's law coefficients ($H_2O_2$, $h \approx 1.92 \times 10^6$ and $O_3$, $h \approx 0.274$). As in the reaction-diffusion simulations, $H_2O_2$ is depleted in the gas phase near the droplet at the end of pulsing (1 ms), as shown in figure 20. Since the droplet is not quickly saturated, $H_2O_2$ continues to solvate into the droplet throughout the pulsing, increasing the zone of depletion around the droplet. The depletion then requires that the gas phase $H_2O_2$ solvating into the droplet at the surface be replenished with $H_2O_2$ originating in the plasma further from the droplet. A small amount of depletion of gas phase $O_3$ also occurs around the droplet, shown in figure 20, as the droplet is saturated with $O_{3aq}$. (The solvated $O_{3aq}$ does originate from the gas phase directly adjacent to the surface.) However, due to ozone's low Henry's law constant, saturation of the droplet quickly occurs, solvation ceases and the depletion around the droplet is compensated by diffusion from outside the depletion zone.

These trends determine which species will have highest aqueous densities at the end of pulsing. We predict that increasing pulse repetition frequencies (PRF) will increase local densities of gas phase precursors which will disproportionately favor increases in the densities of high-$h$ species. The local depletion around the droplet of gas phase species having high-$h$ which occurs by transport into the droplet between pulses will be replenished by production of that species during the following discharge pulse. The replenishment enables solvation to continue with each pulse. Since significant depletion regions do not form for low-$h$ species, higher PRF will not influence the densities of their liquid-phase counterparts to the

same degree as high-$h$ species. Increases in the aqueous equilibrium density of low-$h$ species will occur only by increasing the density of its gas phase density partner.

The diameter of the droplet is an important factor which influences solvation rates. The transport of solvated species through the liquid bulk is driven by diffusion. Solvation into the droplet is determined by equilibrium at the surface. Solvation can continue into the droplet if the surfaces densities decrease below their equilibrium values by reactions at the surface or by transport from the surface into the volume. The time between pulses may then have consequences. For example, consider high PRF excitation having a short interpulse period. If the droplet surface layer is still saturated due to lack of time for the solvated species to diffuse into the interior by the time of the next discharge pulse, then solvation will not occur. At low PRF (long interpulse period), there may be sufficient time for the saturated species at the surface to diffuse into the droplet, thereby enabling solvation during the next pulse.

When computing aqueous densities with an afterglow period extending to 50 ms after the discharge pulses, the densities of most liquid-phase species decrease, as shown in figure 19. In the afterglow ($t > 1$ ms) the density of $O_{3aq}$ also decays, a trend not seen with the global modeling. The cause of these trends is shown in figure 21 where the local densities of $H_2O_2$ and $O_3$ directly inside and outside the droplet surface are plotted as a function of time. There are 100 discharge pulses up to 1 ms, followed by afterglow. During the plasma-on period the local densities of both gas phase $O_3$ and $H_2O_2$ begin to saturate at about 0.3 ms. With the density of $O_3$ saturating, the density of $O_{3aq}$ also saturates, characteristic of a low-$h$ species. In spite of the density of $H_2O_2$ saturating, the density of $H_2O_{2aq}$ continues to increase. At this time, the aqueous density of this high-$h$ species is not saturated, and so transport continues into the droplet.

When the plasma is turned-off at 1 ms, the gas-phase precursors cease to be repopulated while also rapidly diffusing away from the center of the reactor where the single, narrow filament was confined. Gas phase reactions may also contribute to depleting these densities. With the local gas phase density decreasing due to diffusion away from the axis, $O_{3aq}$ de-solvates from the surface to maintain equilibrium with the $O_3$ immediately adjacent to the droplet. Since the $H_2O_{2aq}$ density is not saturated at the surface of the droplet (high-$h$), the degree of de-solvation is less than that of $O_{3aq}$. Even with the density of gas phase $H_2O_2$ decreasing adjacent to the droplet, the droplet is not saturated and so the rate of de-solvation is moderate.

In general, a large SVR increases the rate of gas phase solvation into the droplet if the droplet is under-saturated. However, a large SVR will also increase the rate of de-solvation out of the droplet if the droplet is super-saturated. In this example, a high SVR negatively impacts the ability of the liquid to retain solvated species in the afterglow. Combinations of droplets having different SVR, with bursts of plasma pulses at different PRF followed by afterglow may be another means of controlling plasma activated aerosols.
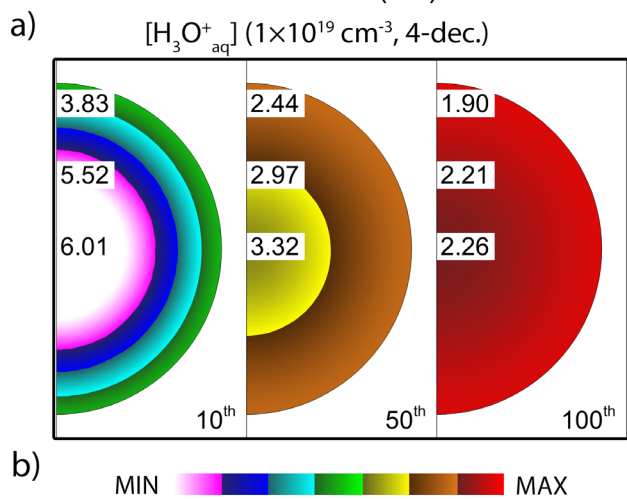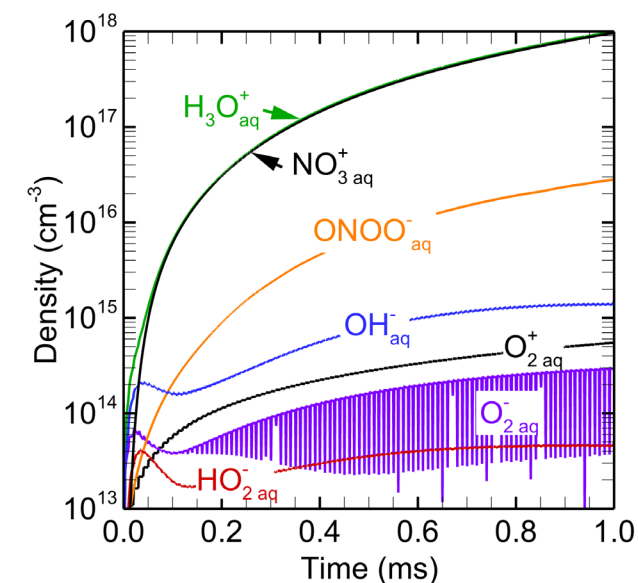
J. Phys. D: Appl. Phys. **52** (2019) 355207

J Kruszelnicki *et al*



**Figure 22.** Properties of aqueous species. (a) Densities of liquid-phase ions as a function of time during pulsing and (b) local densities of $H_3O_{aq}^+$ and local pH after 10, 50 and 100 pulses.

The rates of de-solvation shown here for a single droplet in a single-filament DBD represent a worst-case scenario. The droplet is on the axis of a single discharge filament that repeats in the same location with no discharge producing precursors elsewhere. This geometry produces the maximum density of gas phase precursors in the immediate vicinity of the droplet which then rapidly diffuse away from the droplet during the afterglow. In fact, DBDs usually have arrays of many micro-discharges that produce, on the average, a more uniform distribution of gas phase precursors. Droplets will also be randomly distributed among and between these filaments, resulting in solvation occurring during the afterglow for those droplets receiving reactants produced by distance filaments. The gas phase environment around a given droplet in a random distribution of filaments is likely more stable than portrayed here. Having said that, de-solvation of species from the droplet *will occur* if the density of their gas phase precursors decreases adjacent to the droplet. It is merely a matter of degree.
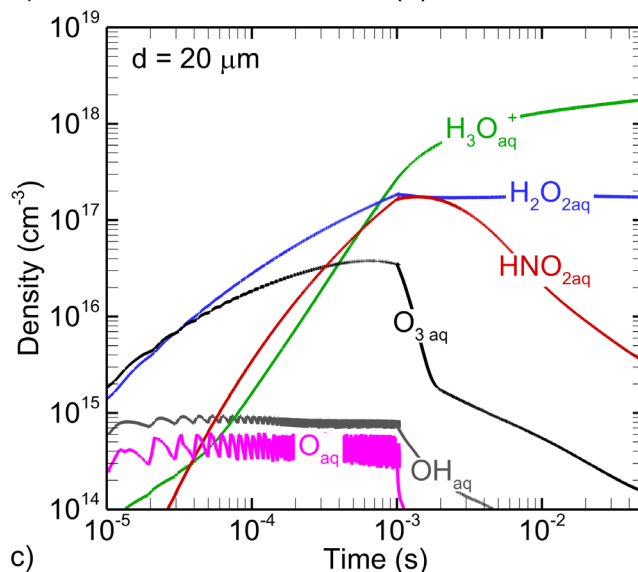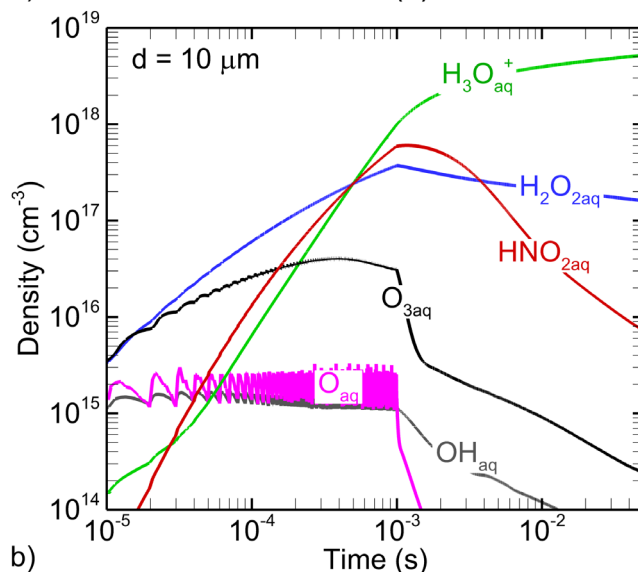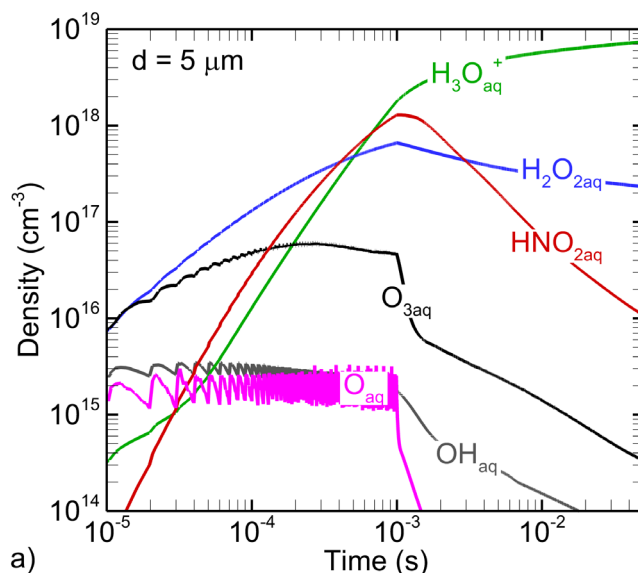


**Figure 23.** Time evolution of selected RONS during pulsing with droplet diameters of (a) 5, (b) 10 and (c) 20 $\mu m$.

J. Phys. D: Appl. Phys. **52** (2019) 355207

J Kruszelnicki *et al*

The densities of most of the aqueous RNS decrease in the afterglow as they undergo reactions and, in some cases, de-solvate, as shown in figure 19(b). The terminal RNS is $NO_{3aq}^-$, which forms from solvation of gas-phase RNS and hydrolysis of acids. Of the several weak and strong acids, $HNO_{2aq}$ dominates for the first 4 ms, with densities reaching $5 \times 10^{17}$ cm$^{-3}$ ($8 \times 10^{-6}$ M) at the end of pulsing at 1 ms. The densities of $N_xO_{yaq}$ species also decrease following pulsing. The density of $NO_{2aq}$, for example, reaches a maximum of $2 \times 10^{15}$ cm$^{-3}$ ($3 \times 10^{-6}$ M) at $t = 1$ ms. Its density at $t = 50$ ms, $2 \times 10^{14}$ cm$^{-3}$ ($3 \times 10^{-7}$ M), is higher than, but comparable to the global modeling results of $4.0 \times 10^{13}$ cm$^{-3}$ at 50 ms.

The densities of these and other charged species during pulsing are shown in figure 22(a). The spatial distributions of hydronium inside the droplet after 10, 50 and 100 pulses are shown in figure 22(b). The charged particle densities are dominated by $NO_{3aq}^-$ and $H_3O_{aq}^+$ with average densities approaching $1 \times 10^{19}$ cm$^{-3}$. $ONOO_{aq}^-$, the species with the next highest density, has a density that is nearly two orders of magnitude lower. Lastly, $O_{2aq}^-$ is more reactive than the other ions, as its density is depleted and replenished with each pulse. $O_{2aq}^-$ is primarily produced by a charge exchange between solvated electrons and dissolved oxygen, which leads to an increase in its density on a pulse-to-pulse basis. The depletion of $O_{2aq}^-$ between pulses is by reactions with $H_3O_{aq}^+$ converting $O_{2aq}^-$ to its acid form, $HO_{2aq}$, reactions with $NO_{aq}$, leading to formation of $NO_{3aq}^-$ and $ONOO_{aq}^-$, and charge exchange with OH.

The distribution of $H_3O_{aq}^+$ in the droplet and the local pH are shown in figure 22(b). These distributions are approximately isotropic, even though the distribution of initial gas-phase species was not. This uniform distribution is a consequence of hydronium being primarily formed by a multi-step process culminating in hydrolysis of $HNO_x$ species. The long time required for these species to form, as well as intra-particle diffusion, smooths initially non-uniform sources. The pH is lowest at the surface of the droplet where the density of $H_3O_{aq}^+$ is highest, decreasing to 1.9 at the end of 100 pulses.

### 5.4. Droplet diameter

The base case repeated with droplets having diameters of $d = 5$ $\mu$m and $d = 20$ $\mu$m to further investigate the influence of the SVR on the liquid kinetics. The volume-averaged densities during pulsing and afterglow of selected RONS are in figure 23. The smaller droplets have higher average aqueous densities due to increased rates of solvation relative to their volume (larger SVR). For example, the density of $OH_{aq}$ has a strong dependence on droplet diameter. At the end of the plasma-on period, the density of $OH_{aq}$ scales inversely with droplet diameter, $2 \times 10^{16}$ cm$^{-3}$ ($3 \times 10^{-5}$ M) for $d = 5$ $\mu$m and $6 \times 10^{15}$ cm$^{-3}$ ($1 \times 10^{-5}$ M) for $d = 20$ $\mu$m. This scaling is not explained by changes in the discharge, as the average density of OH in the vicinity of the droplet oscillated between $3 \times 10^{12}$ cm$^{-3}$ and $5 \times 10^{12}$ cm$^{-3}$ for all droplet sizes. In all cases, the hydroxyl density was highest at the surface ($\approx 10^{17}$ cm$^{-3}$, $2 \times 10^{-4}$ M) and decreased towards the center of the
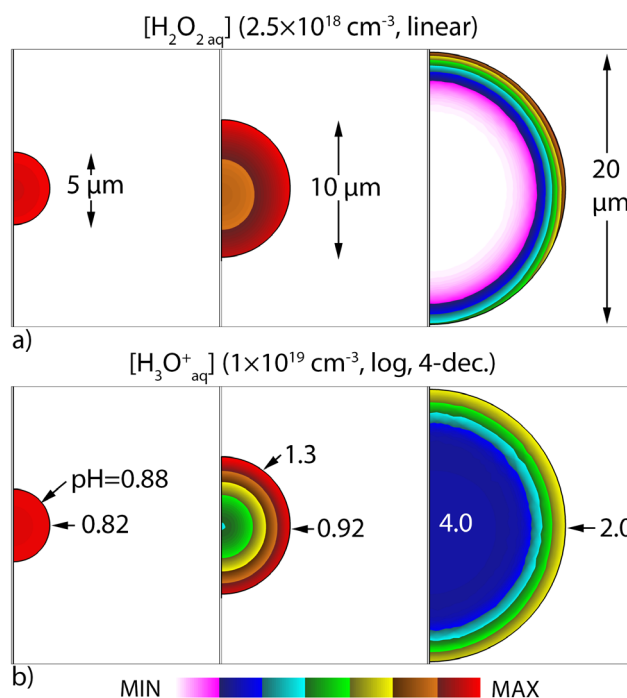


**Figure 24.** Distributions of the densities of (a) $H_2O_{2aq}$ and (b) $H_3O_{aq}^+$ at the end of pulsing for droplet diameters of 5, 10 and 20 $\mu$m. Values of pH are indicated by numerical labels in (b).

droplet. The density of $OH_{aq}$ at the center of the droplet was two orders of magnitude smaller for the 20 $\mu$m droplet, and one order of magnitude smaller for the 5 $\mu$m droplet when compared to the surface. In addition to longer transport times to reach the center of the droplet, $OH_{aq}$ is depleted during transport by the formation of $H_2O_{2aq}$.

At the end of the pulse-on period ($t = 1$ ms), the density of $H_2O_{2aq}$ also has a strong dependence on droplet diameter, higher for smaller droplets, due to the increased relative rates of solvation due to the larger SVR. However, once the plasma was turned off, the average droplet densities become nearly the same. Since none of the droplets are large enough to produce global depletion of $H_2O_2$ during the simulated time, the inventories of gas phase $H_2O_2$ after pulsing are essentially independent of droplet diameter. During the 50 ms of afterglow, there is sufficient time for diffusion to replenish local depletion around the droplet, resulting in the droplets equilibrating to nearly the same $H_2O_{2aq}$ densities in the afterglow. Interestingly, ozone undergoes the opposite process. The $O_{3aq}$ density does reach saturation during pulsing, resulting in similar densities of $O_{3aq}$ at 1 ms, regardless of droplet diameter. However, once the pulsing ends and $O_3$ diffuses throughout the reactor, the local $O_3$ density decreases. For the 1 ms plasma-on period, the intra-droplet distribution of $O_{3aq}$ is disproportionately concentrated near the surface of larger droplets, which then produces a disproportionately higher initial rate of de-solvation. With time, however, the average densities of solvated ozone trend to similar values. A possible means of mitigating this de-solvation would be to collect the droplets into a bulk liquid directly following plasma treatment, therefore abruptly decreasing the SVR.

J. Phys. D: Appl. Phys. **52** (2019) 355207

J Kruszelnicki *et al*

The local distributions of hydrogen peroxide, hydronium, and the local pH at the end of the pulsing period (1 ms) are shown in figure 24 for droplet sizes of 5, 10 and 20 $\mu$m. While the surface densities of $H_2O_{2aq}$ are similar for each droplet size, the densities vary appreciably in the liquid bulk. The diffusion speed through the liquid is approximately three orders of magnitude slower than in the gas at 1 atm, so the liquid species whose production depends primarily on solvation require longer times to equilibrate inside large droplets. The densities of $H_3O_{aq}^+$ at the surface and inside the bulk also vary appreciably as a function of droplet diameter. $H_3O_{aq}^+$ is produced primarily by hydrolysis of acids solvating from the gas phase. These species require several reactions to form in the gas phase. As a result, large fluxes of acids onto the droplet occur later during pulsing, giving less time for diffusion from the surface into the interior. With the shorter diffusion length for $H_3O_{aq}^+$, the average pH at the center of the 5 $\mu$m droplet is 0.82 whereas that for the 20 $\mu$m droplet, pH = 4.0.

## 6. Concluding remarks

The chemical activation of water droplets by atmospheric pressure plasma is sensitive to the droplet diameter, and for individual species, Henry's law constants. Results have been discussed from global and 2D modeling of water droplets activated by repetitively pulsed humid air plasmas. Results from global modeling provided general scaling laws for droplet activation and those from the 2D modeling have shown how the non-uniformities produced by localized microdischarges or localized depletion of gas phase species affect this scaling. By varying the radius of the droplet, the influence of the SVR was shown to be a critical parameter for the transfer of reactivity from the gas-phase into the liquid bulk. Smaller droplets come to equilibrium with the surrounding reactive species in the gas phase in shorter times. This, in turn, enables high Henry's law constant ($h$) species to solvate into the droplet producing higher densities and lower pH. Aqueous densities of high-$h$ species as a function of droplet diameter and density of water droplets are sensitive to depletion of gas phase precursors. Low-$h$ aqueous species come into equilibrium with the gas phase more rapidly, often without depleting local gas-phase densities, and therefore showed a lower degree of dependence on droplet diameter.

Results from the 2D simulations emphasized the importance of the local plasma environment around the droplet on final aqueous densities. In non-uniform discharges as might occur in filamentary DBDs, the gas phase densities adjacent to the droplets may decrease due to diffusion between pulses (or after the discharge terminates). A droplet saturated with an aqueous species during the discharge may become supersaturated after the discharge terminates, leading to rapid de-solvation, and more so for droplets with large SVR. Rates of solvation (and de-solvation) also depend on the aqueous densities on the surface of the droplet, which may be very different from the interior of the droplet. Following termination of the discharge, saturated aqueous densities at the surface of the droplet may decrease because of transport both out of the droplet (de-solvation) and diffusion into the interior.

These dependencies of aqueous densities on droplet size and Henry's law constant provide guidance on how to activate mists of droplets, where the diameter and density of droplets are variables. Total inventories of aqueous species can be separately optimized, providing a control mechanism for chemical activation of liquids.

## Appendix. Henry's law equilibration time

In this appendix, the equilibration time $\tau$ for a gas phase species solvating into a liquid droplet producing a final aqueous density is derived. Beginning with equation (4) and ignoring reactions and evaporation,

$$\frac{dn_l}{dt} = \frac{Dn_g}{\Lambda^2} f_l S_l \frac{V_g}{V_l} \tag{A.1}$$

where $n_l$ is the number density of the species in the liquid, and $n_g$ is the number density of the species in the gas phase. $D$ is the diffusion coefficient, $f_l$ is the fractional area of the liquid in contact with the plasma, $\Lambda$ is the diffusion length of reactants to the droplet, and $S_l$ is the reaction probability of the gas phase species with the liquid. Substituting equation (2) for $S_l$ and assuming the liquid is not oversaturated,

$$\frac{dn_l}{dt} = \frac{Dn_g}{\Lambda^2} f_l \frac{hn_g - n_l}{hn_g} \frac{V_g}{V_l}, \tag{A.2}$$

$$\frac{dn_l}{dt} = \frac{Df_l}{\Lambda^2} \frac{hn_g - n_l}{h} \frac{V_g}{V_l}. \tag{A.3}$$

Neglecting reactions, the total number of molecules should be conserved. Assume at $t = 0$ the liquid density is zero and the gas density is $n_{g0}$.

$$V_g n_{g0} = V_g n_g + V_l n_l \tag{A.4}$$

$$n_g = n_{g0} - \frac{V_l}{V_g} n_l. \tag{A.5}$$

Inserting equation (A.5) into (A.3) to eliminate $n_g$, we have

$$\frac{dn_l}{dt} = \frac{Df_l}{\Lambda^2} \frac{h\left(n_{g0} - \frac{V_l}{V_g}n_l\right) - n_l}{h} \frac{V_g}{V_l}. \tag{A.6}$$

$$\frac{dn_l}{dt} = \frac{Df_l}{\Lambda^2} \left(n_{g0} - \frac{V_l}{V_g}n_l - \frac{n_l}{h}\right) \frac{V_g}{V_l}, \tag{A.7}$$

$$\frac{dn_l}{dt} = \frac{Df_l}{\Lambda^2} \left(\frac{V_g}{V_l}n_{g0} - n_l - \frac{V_g n_l}{V_l h}\right), \tag{A.8}$$

J. Phys. D: Appl. Phys. **52** (2019) 355207

J Kruszelnicki *et al*

$$\frac{dn_l}{dt} = \frac{Df_l}{\Lambda^2}\frac{V_g}{V_l}n_{g0} - \frac{Df_l}{\Lambda^2}\left(\frac{V_g}{V_lh}+1\right)n_l. \qquad (A.9)$$

Integrating equation (A.9) with the initial condition $n_l(t=0)=0$, we can solve for the integration constant,

$$n_l(t) = \frac{hn_{g0}}{1+\frac{hV_l}{V_g}}\left(1-e^{-t/\tau}\right), \qquad (A.10)$$

$$\tau = \frac{\Lambda^2}{Df_l\left(\frac{V_g}{hV_l}+1\right)}. \qquad (A.11)$$

$\tau$ is the characteristic timescale to establish Henry's law equilibrium.

## ORCID iDs

Juliusz Kruszelnicki ⓘ https://orcid.org/0000-0003-4596-1780
Amanda M Lietz ⓘ https://orcid.org/0000-0001-6423-5042
Mark J Kushner ⓘ https://orcid.org/0000-0001-7437-8573

## References

[1] Foster J E, Adamovsky G, Nowak Gucker S and Blankson I M 2013 *IEEE Trans. Plasma Sci.* **41** 503
[2] Bruggeman P J *et al* 2016 *Plasma Sources Sci. Technol.* **25** 053002
[3] Dang T H, Denat A, Lesaint O and Teissedre G 2009 *Eur. Phys. J. Appl. Phys.* **47** 22818
[4] Foster J E, Mujovic S, Groele J and Blankson I M 2018 *J. Phys. D: Appl. Phys.* **51** 293001
[5] Ke Z, Thopan P, Fridman G, Miller V, Yu L, Fridman A and Huang Q 2017 *Clin. Plasma Med.* **7–8** 1–6
[6] Graves D B 2017 *IEEE Trans. Radiat. Plasma Med. Sci.* **1** 281
[7] McCombs G B and Darby M L 2010 *Int. J. Dent. Hyg.* **8** 10
[8] Rossi F, Kylián O, Rauscher H, Hasiwa M and Gilliland D 2009 *New J. Phys.* **11** 115017
[9] Nosenko T, Shimizu T and Morfill G E 2009 *New J. Phys.* **11** 115013
[10] Partecke L I *et al* 2012 *BMC Cancer* **12** 473
[11] Kong M G, Kroesen G, Morfill G, Nosenko T, Shimizu T, van Dijk J and Zimmermann J L 2009 *New J. Phys.* **11** 115012
[12] Xu H, Chen C, Liu D, Xu D, Liu Z, Wang X and Kong M G 2017 *J. Phys. D: Appl. Phys.* **50** 245201
[13] Parvulescu V I, Magureanu M and Lukes P 2012 *Plasma Chemistry and Catalysis in Gases and Liquids* (Weinheim: Wiley)
[14] Winter J *et al* 2014 *J. Phys. D: Appl. Phys.* **47** 285401
[15] Oury T D, Tatro L, Ghio A J and Piantadosi C A 1995 *Free Rad. Res.* **23** 537
[16] Beckman J S and Koppenol W H 1996 *Am. J. Physiol.* **271** C1424
[17] Beckman J S, Beckman T W, Chen J, Marshall P A and Freeman B A 1990 *Proc. Natl Acad. Sci.* **87** 1620
[18] Glaze W H, Kang J W and Chapin D H 1987 *Ozone Sci. Eng.* **9** 335
[19] Broséus R, Vincent S, Aboulfadl K, Daneshvar A, Sauvé S, Barbeau B and Prévost M 2009 *Water Res.* **43** 4707
[20] Lukes P and Locke B R 2005 *J. Phys. D: Appl. Phys.* **38** 4074
[21] Oehmigen K, Hähnel M, Brandenburg R, Wilke C, Weltmann K D and von Woedtke T 2010 *Plasma Process. Polym.* **7** 250
[22] Machala Z, Chládeková L and Pelach M 2010 *J. Phys. D: Appl. Phys.* **43** 222001
[23] Malik M A 2010 *Plasma Chem. Plasma Process.* **30** 21
[24] Bruggeman P and Leys C 2009 *J. Phys. D: Appl. Phys.* **42** 053001
[25] Sommers B S and Foster J E 2014 *Plasma Sources Sci. Technol.* **23** 015020
[26] Schaper L, Graham W G and Stalder K R 2011 *Plasma Sources Sci. Technol.* **20** 034003
[27] Aoki H, Kitano K and Hamaguchi S 2008 *Plasma Sources Sci. Technol.* **17** 025006
[28] Foster J E, Weatherford B, Gillman E and Yee B 2010 *Plasma Sources Sci. Technol.* **19** 025001
[29] Lai J, Petrov V and Foster J E 2018 *IEEE Trans. Plasma Sci.* **46** 875
[30] Neyts E C, Yusupov M, Verlackt C C and Bogaerts A 2014 *J. Phys. D: Appl. Phys.* **47** 293001
[31] Yusupov M, Neyts E C, Simon P, Berdiyorov G, Snoeckx R, Van Duin A C T and Bogaerts A 2014 *J. Phys. D: Appl. Phys.* **47** 025205
[32] Gopalakrishnan R, Kawamura E, Lichtenberg A J, Lieberman M A and Graves D B 2016 *J. Phys. D: Appl. Phys.* **49** 295205
[33] Iqbal M M, Stallard C P, Dowling D P and Turner M M 2015 *Plasma Process. Polym.* **12** 1256
[34] Grinevich V I, Kvitkova E Y, Plastinina N A and Rybkin V V 2011 *Plasma Chem. Plasma Process.* **31** 573
[35] Jin X, Bai H, Wang F, Wang X and Ren H 2011 *IEEE Trans. Plasma Sci.* **39** 1099
[36] Locke B R, Sato M, Sunka P, Hoffmann M R and Chang J S 2006 *Ind. Eng. Chem. Res.* **45** 882
[37] Kovacevic V, Dojcinovic B P, Jovic M, Roglic G M, Obradovic B M and Kuraica M M 2017 *J. Phys. D: Appl. Phys.* **50** 155205
[38] Kovalova Z, Leroy M, Kirkpatrick M J, Odic E and Machala Z 2016 *Bioelectrochemistry* **112** 91
[39] Patel K, Mannsberger A, Suarez A, Patel H, Kovalenko M, Fridman A, Miller V and Fridman G 2016 *Plasma Med.* **6** 447
[40] Wandell R J and Locke B R 2014 *Ind. Eng. Chem. Res.* **53** 609
[41] Locke B R and Shih K 2011 *Plasma Sources Sci. Technol.* **20** 034006
[42] Lietz A M and Kushner M J 2016 *J. Phys. D: Appl. Phys.* **49** 425204
[43] Davidovits P, Kolb C E, Williams L R, Jayne J T and Worsnop D R 2011 *Chem. Rev.* **111** PR76
[44] Zientara M, Jakubczyk D, Derkachov G, Kolwas K and Kolwas M 2005 *J. Phys. D: Appl. Phys.* **38** 1978
[45] Muller B and Heal M R 2002 *Phys. Chem. Chem. Phys.* **4** 3365
[46] Van Doren J M, Watson L R, Davidovits P, Worsnop D R, Zahniser M S and Kolb C E 1990 *J. Phys. Chem.* **94** 3265
[47] Heinisch C, Wills J B, Reid J P, Tschudi T and Tropea C 2009 *Phys. Chem. Chem. Phys.* **11** 9720
[48] Sander R 2015 *Atmos. Chem. Phys.* **15** 4399
[49] Norberg S A, Johnsen E and Kushner M J 2015 *Plasma Sources Sci. Technol.* **24** 035026
[50] Tian W, Lietz A M and Kushner M J 2016 *Plasma Sources Sci. Technol.* **25** 055020
[51] Scharfetter D L and Gummel H K 1969 *IEEE Trans. Electron Devices* **16** 64
[52] Lietz A M and Kushner M J 2018 *Plasma Sources Sci. Technol.* **27** 105020
[53] Gallagher J W, Brion C E, Samson J A R and Langhoff P W 1988 *J. Phys. Chem. Ref. Data* **17** 9
[54] Smith F L and Harvey A H 2007 *Chem. Eng. Prog.* **103** 33
[55] Fernández-Prini R, Alvarez J L and Harvey A H 2003 *J. Phys. Chem. Ref. Data* **32** 903

J. Phys. D: Appl. Phys. **52** (2019) 355207

J Kruszelnicki *et al*

[56] O'Sullivan D W, Lee M, Noone B C and Heikes B G 1996 *J. Phys. Chem.* **100** 3241

[57] Tonini S and Cossali G E 2016 *Int. J. Heat Mass Transfer* **92** 184

[58] Kuchma A E, Shchekin A K and Martyukova D S 2016 *J. Aerosol Sci.* **102** 72

[59] Gibou F and Fedkiw R 2005 *J. Comput. Phys.* **202** 577

[60] Djikaev Y S and Tabazadeh A 2003 *J. Geophys. Res.* **108** 4689

[61] Vácha R, Slavíček P, Mucha M, Finlayson-Pitts B J and Jungwirth P 2004 *J. Phys. Chem.* A **108** 11573

[62] Markosyan A H, Luque A, Gordillo-Vázquez F J and Ebert U 2014 *Comput. Phys. Commun.* **185** 2697

[63] Van Gaens W and Bogaerts A 2014 *Plasma Sources Sci. Technol.* **23** 035015

[64] Lietz A M and Kushner M J 2018 *J. Appl. Phys.* **124** 153303

[65] Fehsenfeld F C, Mosesman M and Ferguson E E 1971 *J. Chem. Phys.* **55** 2115

[66] Light T S, Licht S, Bevilacqua A C and Morash K R 2005 *Electrochem. Solid-State Lett.* **8** E16

[67] Malmberg C G and Maryott A A 1956 *J. Res. Natl Bur. Stand.* **56** 2641

[68] Grashchenkov S I and Grigoryev A I 2011 *Fluid Dyn.* **46** 437

[69] Maguire P D *et al* 2015 *Appl. Phys. Lett.* **106** 224101

[70] Young R M and Neumark D M 2012 *Chem. Rev.* **112** 5553

[71] Rumbach P, Bartels D M, Sankaran R M and Go D B 2015 *Nat. Commun.* **6** 7248

[72] Taflin D C, Ward T L and Davis E J 1989 *Langmuir* **5** 376